J. Fluid Mech. (1988), *vol.* 194, *pp.* 101–132
Printed in Great Britain

Spectral study of the laminar–turbulent transition in spherical Couette flow

By KOICHI NAKABAYASHI AND YOICHI TSUCHIDA
Department of Mechanical Engineering, Nagoya Institute of Technology, Nagoya 466, Japan

(Received 24 July 1987)

The laminar–turbulent transition of the Taylor–Görtler (TG) vortex flow in the clearance between two concentric spheres with only the inner sphere rotating (spherical Couette flow) is investigated by velocity measurement and simultaneous spectral and flow-visualization measurements by measuring the intensity of light scattered by the aluminium flakes used in flow visualization in the case of a relatively small ratio of the clearance to inner-sphere radius (clearance ratio $\beta = 0.14$). An azimuthal velocity component has been measured by a constant-temperature hot-wire anemometer at two different colatitudes (meridian angles) θ; $\theta = 80°$ and $90°$ (the equator). A critical Reynolds number, some transition Reynolds numbers, flow regimes and flow states are obtained by the simultaneous spectral and flow-visualization measurements. The flow state is expressed by the number of toroidal TG vortex cells N, that of spiral TG vortex pairs S_P, the wavenumber of the travelling azimuthal waves on the toroidal TG vortices m and the wavenumber of shear waves S_H. The mean velocity distribution and the characteristic values of the fluctuating velocity, such as autocorrelation coefficient, power spectrum and turbulence intensity (r.m.s. value), are considered over a great range of Reynolds number *Re*. Three kinds of fundamental frequencies of the velocity fluctuation are discovered and their characteristics are clarified by means of the velocity measurement and the simultaneous spectral and flow-visualization measurements. The three kinds of fundamental frequencies expressed by f_S, f_W and f_H correspond to the spiral TG vortices, the travelling azimuthal waves and the shear waves, respectively. These fundamental frequencies are independent of both θ and wall distances from the inner sphere, but depend strongly on *Re*. Although the rotation frequency of the travelling azimuthal waves (or wave speed) in the circular Couette flow decreases monotonically with increasing Reynolds number until it reaches a plateau, the values of the rotation frequencies of the spiral TG vortices, the travelling azimuthal waves and the shear waves in the spherical Couette flow, f_S/S_P, f_W/m and f_H/S_H, are nearly constant as the Reynolds number is increased, and differ slightly from one another.

1. Introduction

In this paper the laminar–turbulent transition is considered for the Taylor–Görtler (TG) vortex flow between two concentric spheres with the inner sphere rotating and the outer sphere at rest (spherical Couette system). This kind of transition, which is called transition by spectral evolution, is similar to the transition in the Taylor vortex flow between two concentric cylinders with only the inner cylinder rotating (circular Couette system), as well as Rayleigh–Bénard convection, where the velocity fluctuation power spectrum changes gradually as a cascade process from a line spectrum to a continuous one by broadening of the initially sharp spectral lines.

Recently, many studies on this kind of transition have been reported except for the case of the spherical Couette system. Although the flow in the spherical Couette system has been investigated by Sawatzki & Zierep (1970), Munson & Menguturk (1975), Wimmer (1976), Waked & Munson (1978), Nakabayashi (1978), Krause (1980), Belyaev *et al.* (1979, 1984), Yavorskaya *et al.* (1980), Bartels (1982), Nakabayashi (1983), Tuckerman (1983), Bühler & Zierep (1983, 1984), Dennis & Quartapelle (1984), Schrauf & Krause (1984), Schrauf (1986) and others over a wide range of Reynolds number which includes the transition from laminar to turbulent flow, the details of the transition by spectral evolution have not been investigated for this system. On the other hand, for the circular Couette system, the measurements of the wave speed (rotation frequency) of the travelling azimuthal waves on the Taylor vortices have been progressively made. And the fundamental frequency of velocity fluctuation was considered by Coles (1965), Yahata (1978, 1979, 1980), Walden & Donnelly (1979), Fenstermacher, Swinney & Gollub (1979), Bouabdallah & Cognet (1980), Gorman & Swinney (1982) and King *et al.* (1984). And the hot-wire measurements of velocity were also reported by Townsend (1984).

For the spherical Couette system, however, Belyaev *et al.* (1984) considered the fundamental frequency of velocity fluctuation for the ratio β of gap to inner-sphere radius greater than 0.4, where no TG vortex is detectable. Because the flow behaviour depends strongly on β for the spherical Couette system, the toroidal TG vortex has not been observed for $\beta > 0.4$ (Waked & Munson 1978, Yavorskaya *et al.* 1980). Schrauf (1986) investigated the influence of β on the first instability of the spherical Couette flow, and obtained the theoretical results that no TG vortex exists for $\beta \geqslant 0.48$. Wimmer (1976) was the only investigator to report the velocity measured for a small clearance in which the TG vortex is detectable, where neither the fundamental frequency of velocity fluctuation nor development of turbulence was considered.

The present study has focused on the laminar–turbulent transition of the TG vortex flow in the spherical Couette system under the condition that the Reynolds number is increased stepwise by a quasi-static increase of the rotation frequency of the inner sphere from zero, when the final flow field of the last step is used for the initial condition. The vortex flows encountered as the Reynolds number is increased are a toroidal one, a toroidal and spiral one, a wavy toroidal and spiral one, a toroidal and spiral one, a toroidal one, a turbulent wavy toroidal one with shear waves and a turbulent toroidal one. The value of $\beta = 0.14$ is chosen in this experiment, because many studies on the fundamental frequency of velocity fluctuation have been reported for $\beta \approx 0.14$ in the case of the circular Couette–Taylor vortex flow. The toroidal TG vortex occurring near the equator in the spherical Couette system is similar to the Taylor vortex in the circular Couette system. But the travelling azimuthal waves on the toroidal TG vortices are influenced by the Ekman boundary-layer effect for the spherical Couette system, so that their wave speed corresponds to that of the travelling azimuthal waves on the Taylor vortices for the finite cylinder in the circular Couette system, where the end effect appears. For the spherical Couette system, the special vortex or flow state, which is different from the circular Couette–Taylor vortex, is observed towards the pole from the equator. In the spherical Couette system, as mentioned above, various disturbances, partly similar to and partly different from those in the circular Couette system, are observed in the transition to turbulence. Consequently, it is important that the various disturbances

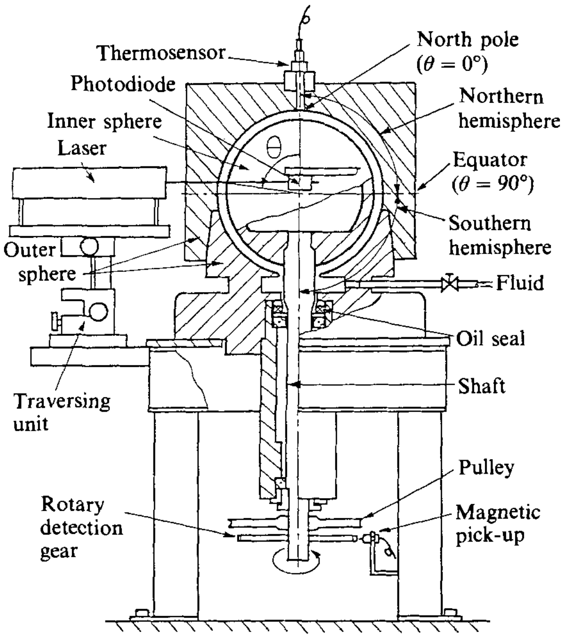

FIGURE 1. Experimental apparatus for the simultaneous spectral and flow-visualization measurements by measuring the intensity of laser light scattered by the aluminium flakes used in flow visualization.

observed in the circular and spherical Couette systems are compared with each other.

In §2 we describe the experimental techniques used for the identification of the fundamental frequencies of velocity fluctuation. In §3 we explain the flow regimes over the *Re* range pursued in the present experiment and the experimental results. The fundamental frequencies are discussed and compared with other experiments in §4. Development to chaos is described in §5. The conclusions are presented in §6.

2. Experimental techniques

The spherical Couette flow is considered under the condition that the Reynolds number of the flow (i.e. the rotation of the inner sphere) is quasi-statically increased from zero, where the flow regime is uniquely determined by only the Reynolds number. If the Reynolds number is increased with a given acceleration rate, the flow regime depends not only on the Reynolds number but also on the acceleration rate.

The fundamental frequency of velocity fluctuation cannot always be identified by only the spectral analysis of the velocity fluctuation. When the velocity fluctuation has plural fundamental frequencies, many frequency components of their integer–linear combinations are produced by their nonlinear interaction. Therefore, it is difficult to identify the fundamental frequencies among them correctly. Thus, we have made not only the velocity measurement by a hot-wire anemometer but also simultaneous spectral and flow-visualization measurements by measuring the intensity of laser light scattered by the aluminium flakes suspended in the working fluid. The fundamental frequency could be identified by comparing the results of

Measurements	Radius Inner sphere R_1 (mm)	 Outer sphere R_2 (mm)	Clearance ratio β	Critical Reynolds number Re_c
Spectral and flow-visualization	76.89 ± 0.01	87.65 ± 0.01	0.1399	880
Velocity		87.68 ± 0.005	0.1403	

TABLE 1. Dimensions of the inner and outer spheres, the ratios and the critical Reynolds number in the two concentric-sphere systems.

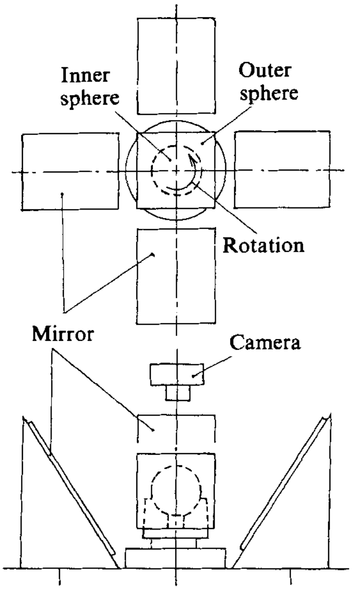

FIGURE 2. Mirror arrangement for simultaneous observation of all spiral TG vortices, travelling azimuthal waves or shear waves around the annulus.

these measurements. The methods of the simultaneous spectral and flow-visualization measurements and the velocity measurement are described below in detail.

2.1. *Simultaneous spectral and flow-visualization measurements*

The experimental apparatus for the simultaneous spectral and flow-visualization measurements is shown in figure 1. The values of the radii R_1 and R_2 of the inner and outer spheres, the clearance ratio β and the critical Reynolds number Re_c are given in table 1. The clearance ratio β is defined as $(R_2 - R_1)/R_1$, and the Reynolds number Re as $2\pi f_0 R_1^2/\nu$, where f_0 is the rotation frequency of the inner sphere, and ν the kinematic viscosity of the fluid. The value of the critical Reynolds number, $Re_c = 880$, was obtained by the flow-visualization measurement. The accuracies of the whip of the rotating inner sphere and the concentricity of the inner and outer spheres were assured to be within ±0.015 mm and ±0.01 mm, respectively. Water and glycerol–water solution of 50% concentration were used for working fluids. Flow patterns were visible in the working fluids at room temperature using a suspension of small aluminium flakes that align with the flow. In order to clarify the flow state, the whole spherical surface view and the meridian cross-section of the spherical annulus were observed by front lighting and slit illumination, respectively. Furthermore, in order to determine the evolutions of the spiral and wave patterns such as the spiral TG vortices, the shear waves and the travelling azimuthal waves, four mirrors were used as shown in figure 2 and the entire annulus was observed at all times. This technique was employed in the circular Couette system by Gorman & Swinney (1982).

The laser light (about 0.9 mm diameter) was illuminated in the flow normal to the meridian cross-section of the spherical annulus, as seen in figure 1, and the intensity of the laser light scattered by the aluminium flakes was detected by the photodiode with a pinhole (0.7 mm diameter) located alongside the laser light. The photocurrent was digitized and recorded in the computer. The power spectrum $P_L(f)$ was computed from time series records, where f is the non-dimensional frequency defined by $\hat{f}/\hat{f}_0$. The frequency of fluctuation $\hat{f}$ is expressed in units of the inner sphere rotation frequency $\hat{f}_0$. The power spectrum of the scattered-light intensity can be obtained at any colatitude θ by changing the locations of both the laser light and the photodiode. The non-dimensional spectral resolution $\Delta f\,(=\Delta\hat{f}/\hat{f}_0=(2\hat{f}_N/N_d)/\hat{f}_0)$, where $\hat{f}_N$ and N_d are the Nyquist frequency and the number of the above time-series records, respectively, is about 0.005–0.01 for $\hat{f}_N=(10\text{–}20)\hat{f}_0$ and $N_d=2048$ or 4096.

The fundamental frequency of the velocity fluctuation related to the spiral or wave pattern such as the spiral TG vortices, the shear waves or the travelling azimuthal waves was identified by both the observation of the spiral or wave pattern by eye with a stopwatch or a stroboscope and the spectral analysis of the scattered-light intensity.

2.2. *Velocity measurement*

The schematic of the top view of the experimental apparatus and the measuring system for velocity measurement are illustrated in figure 3(*a*). The values of R_1, R_2 and β of this apparatus are given in table 1. The value of β is almost the same as that in figure 1 (both clearance ratios are about 0.14). The accuracies of the whip of the rotating inner sphere and the concentricity of the inner and outer spheres for this apparatus are of the same order as those in figure 1. The temperature of the working fluid (air) was measured by a thermosensor (thermistor) located at the north pole (the colatitude $\theta=0°$). The rotation of the inner sphere was counted by a digital tachometer, and the increase in the rotation was made so slowly that the transition appeared quasi-statically. The increasing rate $\dot{R}^*$ of a reduced Reynolds number $R^*=Re/Re_C$ was kept to less than 0.0009 1/s. The hot-wire probe and the I-type prong used in the present experiment are shown in figure 3(*b*, *c*). The support of the hot-wire probe was flush with the spherical surface of the outer sphere, as seen in figure 3(*b*). The prong was made as thin as possible, as seen in figure 3(*c*), in order to avoid the influence of the wake behind it.

The output of the hot-wire anemometer (azimuthal velocity component v_ϕ) was amplified, low-pass filtered and sampled by a data recorder or a microcomputer. The mean azimuthal velocity $\bar{v}_\phi$, the power spectrum $P(f)$, the autocorrelation coefficient $R(\tau^*)$ and the turbulence intensity (r.m.s. value) $\hat{v}_\phi=(\overline{\tilde{v}_\phi^2})^{0.5}$ of the fluctuating azimuthal velocity $\tilde{v}_\phi$, were calculated from the output. The power spectrum of the velocity fluctuation was calculated by FFT, and the autocorrelation coefficient was obtained by the inverse FFT of the spectrum. The non-dimensional spectral

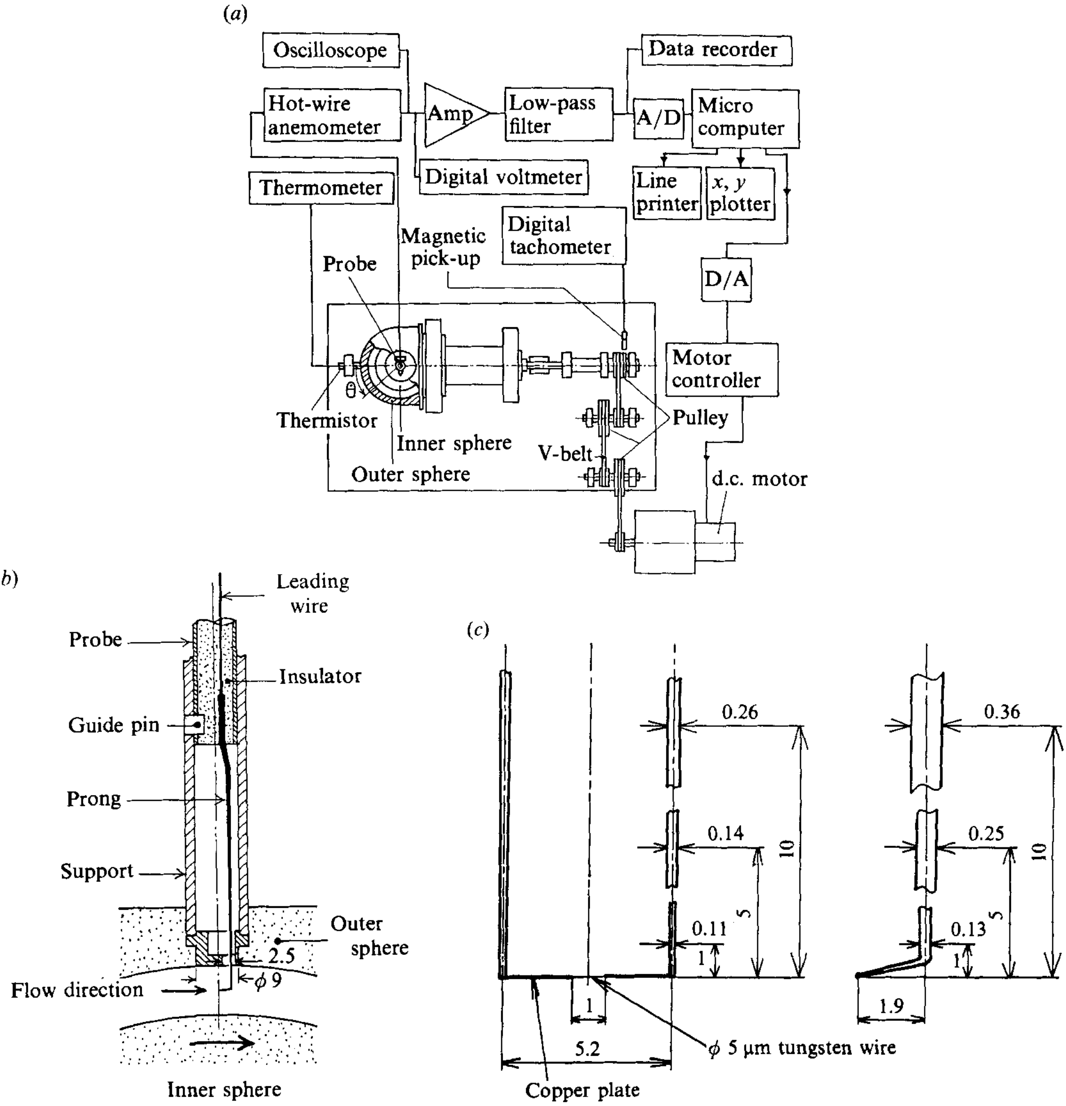

FIGURE 3. Experimental apparatus and hot-wire anemometry for the velocity measurement. (a) Schematic of experimental apparatus and measuring system. (b) Schematic of hot-wire probe. (c) Geometry of hot-wire prong.

resolution Δf for the velocity fluctuation is 0.005–0.01, the same as for scattered-light intensity. But occasionally the resolution is 0.0024 ($N_d = 8192$) for a high resolution spectrum.

3. Outline of experimental results

3.1. *Flow regimes*

Seven flow regimes (IIT, $\mathrm{IITS_N}$, $\mathrm{IIIWTS_N}$, $\mathrm{IIITS_N}$, IIIT, $\mathrm{IVWTS_h}$ and IVT) are successively obtained when the reduced Reynolds number R^* is quasi-statically

Flow regime	Characteristics	R_C^*, R_i^*	N	S_P, S_H	f_S, f_H	m	f_W
IIT	Laminar flow + toroidal TG vortex + secondary flow	$R_C^* = 1$	2	—	—	—	—
IITS_N	Laminar flow + toroidal and spiral TG vortices + secondary flow	$R_{1a}^* = 1.13$ $R_{1b}^* = 1.49$	2 2	$S_P = 3$ $S_P = 2$	$f_{S1} = 1.315 \pm 0.009$ $f_{S2} = 0.854 \pm 0.006$	— —	— —
IIIWTS_N	Laminar flow + wavy toroidal and spiral TG vortices + secondary flow	$R_{2a}^* = 1.71$ $R_{2b}^* = 1.93$ $R_{2c}^* = 2.80$	2 2 2	$S_p = 2$ $S_p = 1$ $S_P = 1$	$f_{S2} = 0.851 \pm 0.004$ $f_{S3} = 0.427 \pm 0.003$ $f_{S3} = 0.426 \pm 0.004$	$m = 6$ $m = 6$ $m = 5$	$f_{W1} = 2.648 \pm 0.009$ $f_{W1} = 2.695 \pm 0.048$ $f_{W2} = 2.256 \pm 0.027$
IIITS_N	Laminar flow + toroidal and spiral TG vortices + secondary flow	$R_3^* = 5.05$	2	$S_P = 1$	$f_{S3} = 0.436 \pm 0.014$	—	—
IIIT	Laminar flow + toroidal TG vortex with strong circulation + secondary flow	R_4^*	2	—	—	—	—
IVWTS_h	Turbulent flow + wavy toroidal TG vortex + secondary flow with shear waves	$R_{5a}^* = 10.5$ $R_{5b}^* = 14.2$	2 2	$S_H = 14$ $S_H \approx 6$	$f_{H1} = 7.763 \pm 0.063$ $f_{H2} = 3.000 \pm 0.015$	$m = 1$ $m = 1$	$f_{W3} = 0.495 \pm 0.013$ $f_{W3} = 0.478 \pm 0.019$
IVT	Fully developed turbulent flow + toroidal TG vortex + secondary flow	$R_6^* = 19$	2	—	—	—	—

TABLE 2. Regime and state transitions, their transition Reynolds numbers, and the values of the fundamental frequencies in each flow regime and flow state, when the Reynolds number is quasi-statically increased to the largest Reynolds number ($R_{max}^* = 59$) in the present experiment

increased over the critical Reynolds number ($R_C^* = 1$) to the largest Reynolds number ($R_{max}^* = 59$) pursued in the present experiment. Their characteristics, flow states (N, S_P, m and S_H), fundamental frequencies (f_S, f_W and f_H) and transition Reynolds numbers R_i^* (i = 1a, 1b, 2a, 2b, 2c, 3, 4, 5a, 5b and 6) are given in table 2. The variables N, S_P, m and S_H are the cell number of toroidal TG vortex cells in both hemispheres, the number of pairs of spiral TG vortices in each hemisphere, the wavenumber of travelling azimuthal waves on the toroidal TG vortices, and the

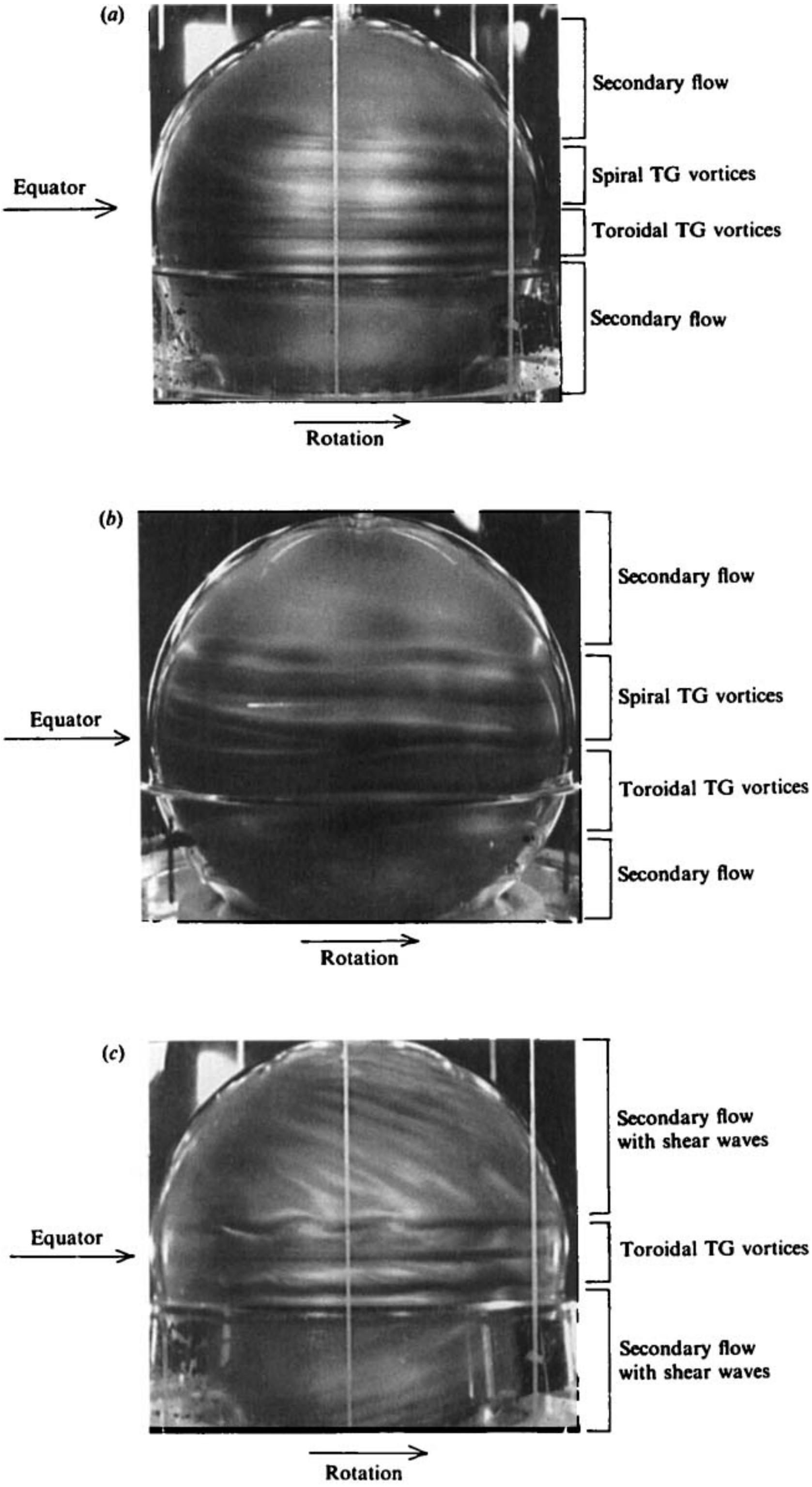

FIGURE 4. For caption see facing page.

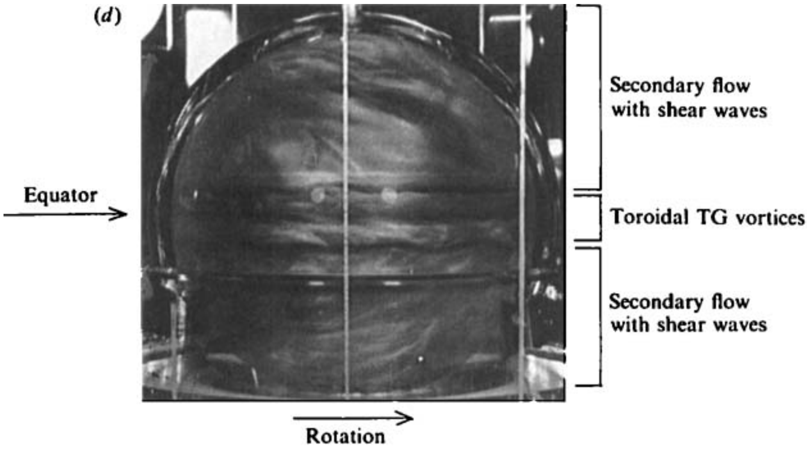

FIGURE 4. Photographs of typical flows observed in some flow regimes taken by front lighting. (*a*) IITS$_N$($N = 2$, $S_P = 3$) at $R^* = 1.18$; laminar toroidal and spiral TG vortices. (*b*) IIIWTS$_N$ ($N = 2$, $S_P = 1$, $m = 6$) at $R^* = 2.15$; wavy toroidal and spiral TG vortices. (*c*) IVWTS$_h$ ($N = 2$, $m = 1$, $S_H = 14$) at $R^* = 12.7$; turbulent wavy toroidal TG vortices and secondary flow with orderly shear waves. (*d*) IVWTS$_h$ ($N = 2$, $m = 1$, $S_H \approx 6$) at $R^* = 15.9$; turbulent wavy toroidal TG vortices and secondary flow with irregular shear waves.

wavenumber of shear waves observed within the Ekman boundary layer near the outer sphere in each hemisphere, respectively. Among the symbols of the flow regimes, the symbol S$_N$ means that the spiral TG vortices occur only in the northern hemisphere ($0° < \theta < 90°$). Although the spiral TG vortices occurred in both hemispheres in Nakabayashi's experiment (1983) for $\beta = 0.138$, they occur only in the northern hemisphere in the present experiment for $\beta = 0.14$ (IITS$_N$, IIIWTS$_N$ and IIITS$_N$). The symbol S$_h$ means that the shear waves occur in both northern and southern ($90° < \theta < 180°$) hemispheres. There are two kinds of transition; regime transition and state transition. The former corresponds to the evolution of flow regime, the latter corresponds to the change for the numbers of the travelling azimuthal waves, the spiral TG vortices or the shear waves. R_i^* (i = 1a, 2a, 3, 4, 5a and 6) are those for the regime transition, while R_i^* (i = 1b, 2b, 2c and 5b) for the state transition, and their values are obtained by the simultaneous spectral and flow-visualization measurements.

The photographs of typical flows observed in some flow regimes taken by front lighting are shown in figure 4(*a–d*). Figure 4(*a*) shows the photograph in the flow regime IITS$_N$. The schematic for the same regime given by Nakabayashi (1983) is shown in figure 12(*a*). A pair of toroidal TG vortices near the equator and three pairs of spiral TG vortices in the northern hemisphere can be seen. The spiral TG vortices extend towards the north pole, and disappear in the secondary flow. They rotate about the axis of the inner sphere with a constant frequency. Figure 4(*b*) shows the photograph in the flow regime IIIWTS$_N$. The schematic for the same regime is shown in figure 12(*b*). Six travelling azimuthal waves were observed on a pair of toroidal vortices near the equator. A pair of wavy spiral TG vortices was also observed in the northern hemisphere. Figure 4(*c*) shows the photograph in the flow regime IVWTS$_h$ whose schematic is shown in figure 12(*c*). One travelling azimuthal wave appeared on a pair of toroidal TG vortices. And fourteen orderly shear waves, which

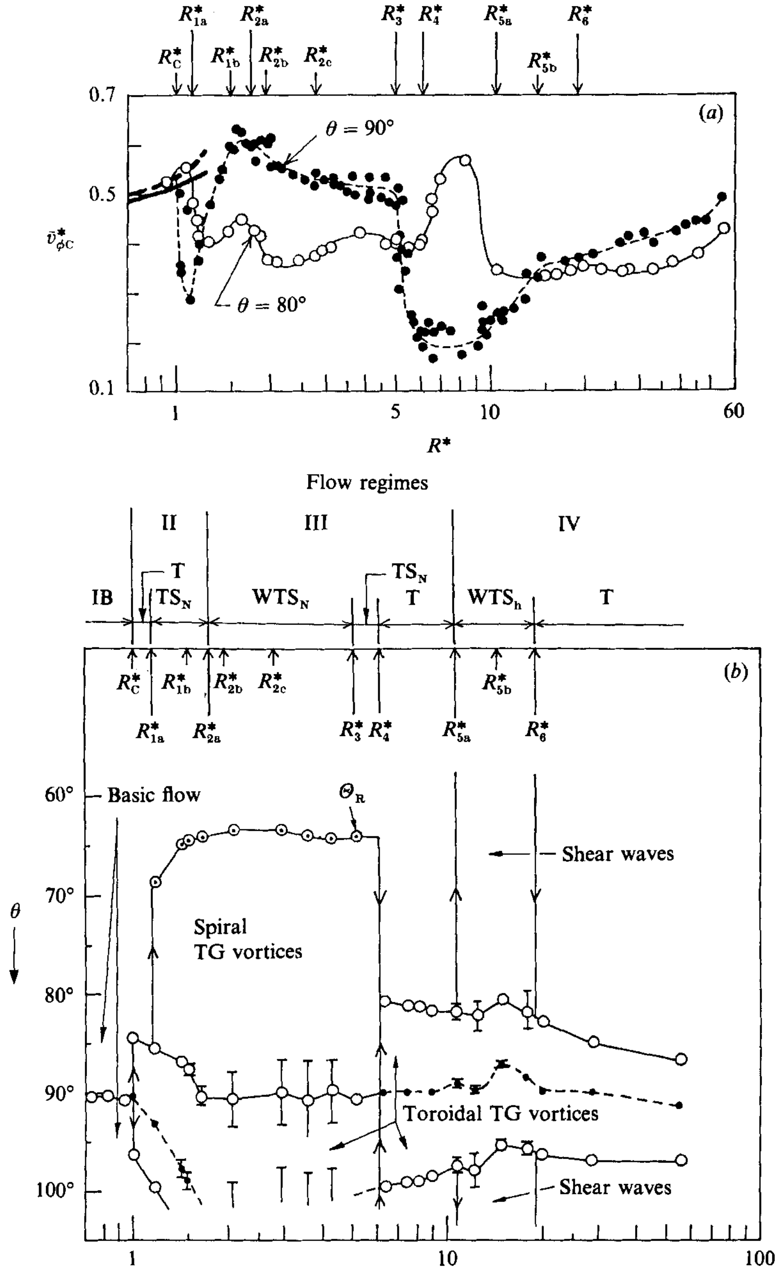

FIGURE 5. Reynolds-number dependences of the mean azimuthal velocity components in the centre of the clearance at the colatitudes $\theta = 80°$ and $90°$ and the meridian coordinate θ of the sources (outflow-vortex boundaries) and/or sinks (inflow-vortex boundaries) of the toroidal cells observed on the inner sphere in a meridian cross-section of spherical annulus. (*a*) Reynolds-number dependences of the mean azimuthal velocity components in the centre of the clearance at ○, $\theta = 80°$ and ●, $\theta = 90°$. The heavy solid and broken lines show the theoretical dependences at $\theta = 80°$ and $90°$, respectively, for the laminar basic flow calculated by Nakabayashi (1976) and Nakabayashi *et al.* (1981). (*b*) Reynolds-number dependences of the meridian coordinate θ of the sources (outflow-vortex boundaries) and/or sinks (inflow-vortex boundaries) of the toroidal cells observed on the inner sphere in a meridian cross-section of spherical annulus: ○, source; ●, sink. The error bar $\overset{\top}{\underset{\bot}{\circ}}$ shows the amplitude of the oscillation. The data Θ_R indicated by ⊙ show the value of θ at which the spiral TG vortices break.

were observed within the secondary flow, ran in spiral fashion from the pole towards the equator, more or less perpendicular to the direction of the secondary flow near the outer sphere. They rotated about the axis of the inner sphere with a constant frequency. The same shear waves were reported by Bühler & Zierep (1984). When R^* increases further, the shear waves become irregular and their wavelength irregularly changes in space and time, as shown in figure 4(*d*), but their wavenumber is estimated to be about 6.

3.2. *Mean velocity distributions*

Before the velocity fluctuation is considered, it is important to discuss the relationship between the velocity profiles and the flow regimes. Figure 5(*a*) shows the Reynolds number dependences of the mean values $\bar{v}^*_{\phi C}$ of the non-dimensional azimuthal velocity components in the centre of the clearance,

$$v^*_{\phi C} = v^*_\phi(\eta = 0.5) = v_\phi(\eta = 0.5)/(2\pi R_1 f_0),$$

at $\theta = 80°$ and $90°$ (the equator). The variable $\eta(=(r-R_1)/(R_2-R_1))$ is the non-dimensional wall distance from the inner sphere, where r is a radial coordinate. Figure 5(*b*) shows the meridian coordinate θ (shown in figure 1) of the sources (outflow-vortex boundaries) and/or sinks (inflow-vortex boundaries) of the toroidal cells observed on the inner sphere in a meridian cross-section of spherical annulus.

Below R^*_C, the values of $\bar{v}^*_{\phi C}$ at $\theta = 80°$ and $90°$ in figure 5(*a*) agree well with the theoretical ones for the laminar basic flow calculated by Nakabayashi (1976) and Nakabayashi *et al.* (1981). In the range $R^*_C \leqslant R^* \lesssim R^*_{1a}$, the value of $\bar{v}^*_{\phi C}$ increases in agreement with the theoretical one at $\theta = 80°$, but decreases from that at $\theta = 90°$. This decrease results from the fact that the fluid particle near the stationary outer sphere, which has a small azimuthal velocity component, moves into the centre region of the clearance, because above R^*_C two toroidal vortex cells appear, so that a sink (inflow-vortex boundary) locates at $\theta = 90°$, as can be seen in figure 5(*b*). For $R^*_{1a} \lesssim R^* \lesssim R^*_{1b}$, the value of $\bar{v}^*_{\phi C}$ decreases at $\theta = 80°$ but increases at $\theta = 90°$, because the toroidal vortex cells move towards the south pole with increasing R^*, i.e. a source leaves from $\theta = 80°$, but approaches $\theta = 90°$, as shown in figure 5(*b*). For $R^*_{1b} \lesssim R^* \lesssim R^*_3$, the values of $\bar{v}^*_{\phi C}$ at $\theta = 80°$ and $90°$ change gradually, according to the locations of the source and sink. The value of $\bar{v}^*_{\phi C}$ is almost constant at $\theta = 80°$ and decreases at $\theta = 90°$ for $R^*_3 \lesssim R^* \lesssim R^*_4$. For $R^*_4 \lesssim R^* \lesssim R^*_{5a}$, it becomes large at $\theta = 80°$ and small at $\theta = 90°$, because the spiral TG vortices disappear and the toroidal vortex cells move towards the north pole, then the source and the sink locate at $\theta = 80°$ and $\theta = 90°$, respectively, as shown in figure 5(*b*). Beyond about R^*_{5a}, both values of $\bar{v}^*_{\phi C}$ at $\theta = 80°$ and $90°$ approach about 0.5, because the chaos grows in the flow. Thus the Reynolds number dependence of $\bar{v}^*_{\phi C}$ can be clearly explained by the inflow or outflow momentum transfer, depending on the location of the toroidal or spiral TG vortex boundary, as described above.

Non-dimensional mean velocity profiles in the azimuthal component at $\theta = 90°$ are shown in figure 6. At $R^* = 0.941$, the mean velocity $\bar{v}^*_\phi$ agrees well with the theoretical one for the laminar basic flow calculated by Nakabayashi (1976) and Nakabayashi *et al.* (1981), and its profile is slightly convex (upward) due to the outflow of the secondary flow. But at $R^* = 1.05$, the profile becomes concave (upward) due to the inflow caused by the sink of TG vortex, as shown in figure 5(*b*). At $R^* = 1.20$ and 1.81, the mean velocity $\bar{v}^*_\phi$ increases only in the centre region of the clearance with increasing R^*. At $R^* = 5.09$, however, it begins to decrease. The value of $\bar{v}^*_\phi$ at $R^* = 6.52$ becomes smaller over the annulus gap because of the inflow

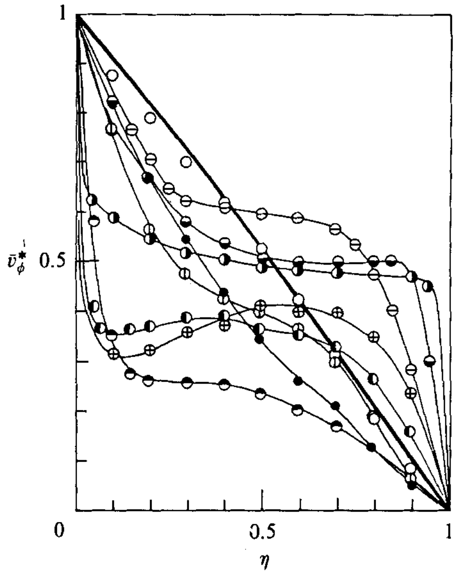

FIGURE 6. Distributions in the clearance of the mean azimuthal velocity component at the equator: ○, $R^* = 0.941$; ●, $R^* = 1.05$; ⦶, $R^* = 1.20$; ⊖, $R^* = 1.81$; ◒, $R^* = 5.09$; ◓, $R^* = 6.52$; ⊕, $R^* = 15.1$; ◐, $R^* = 19.6$; ◑, $R^* = 57.3$. The heavy solid line shows the theoretical distribution at $R^* = 0.941$ for the laminar basic flow calculated by Nakabayashi (1976) and Nakabayashi *et al.* (1981).

momentum transfer, as mentioned above. At $R^* = 15.1$, the profile has a maximum at $\eta \approx 0.6$ and the velocity gradient on the inner sphere becomes great. At $R^* = 19.6$, the profile flattens out in the central region of the gap. At $R^* = 57.3$, the profile approaches that of a turbulent Couette flow and the velocity gradients on the inner and outer spheres become great.

3.3. *Velocity fluctuations*

The temporal dependence of the non-dimensional azimuthal velocity components in the centre of the clearance, $v_{\phi C}^*$, at $\theta = 80°$ and $90°$ is shown in figures 7(*a*) and 7(*b*), respectively. The variable t^* $(=\hat{t}\hat{f}_0)$ is the non-dimensional value of time $\hat{t}$. The values of $1/f_{S1}$, $1/f_{S2}$ etc. are the fundamental periods of the various types of velocity fluctuations described later. At $\theta = 80°$ (figure 7*a*), a sinusoidal fluctuation is first detected, as shown at $R^* = 1.18$ and 1.66. As R^* is increased, a periodic fluctuation ($R^* = 1.81$) appears, and then some noise is added to this fluctuation ($R^* = 2.15$ and 3.91). But the noise almost disappears ($R^* = 5.63$), and then the periodic fluctuations all disappear ($R^* = 6.71$). But with a further increase in R^*, a periodic fluctuation reappears with noise ($R^* = 12.7$ and 15.9), and finally a fully developed turbulence ($R^* = 56.3$) appears. At $\theta = 90°$ (figure 7*b*), the same types of fluctuation as those at $\theta = 80°$ successively appear as R^* is increased, but the waveshapes of the fluctuations differ from those at $\theta = 80°$.

The power spectra of the velocity fluctuations at $\theta = 80°$ are shown in figure 8. At $R^* = 1.18$, the velocity fluctuation power spectrum $P(f)$ contains a single sharp frequency component labelled f_{S1} and its harmonics, which were confirmed to be line spectra within the accuracy of the measurement. The frequency component f_{S1}

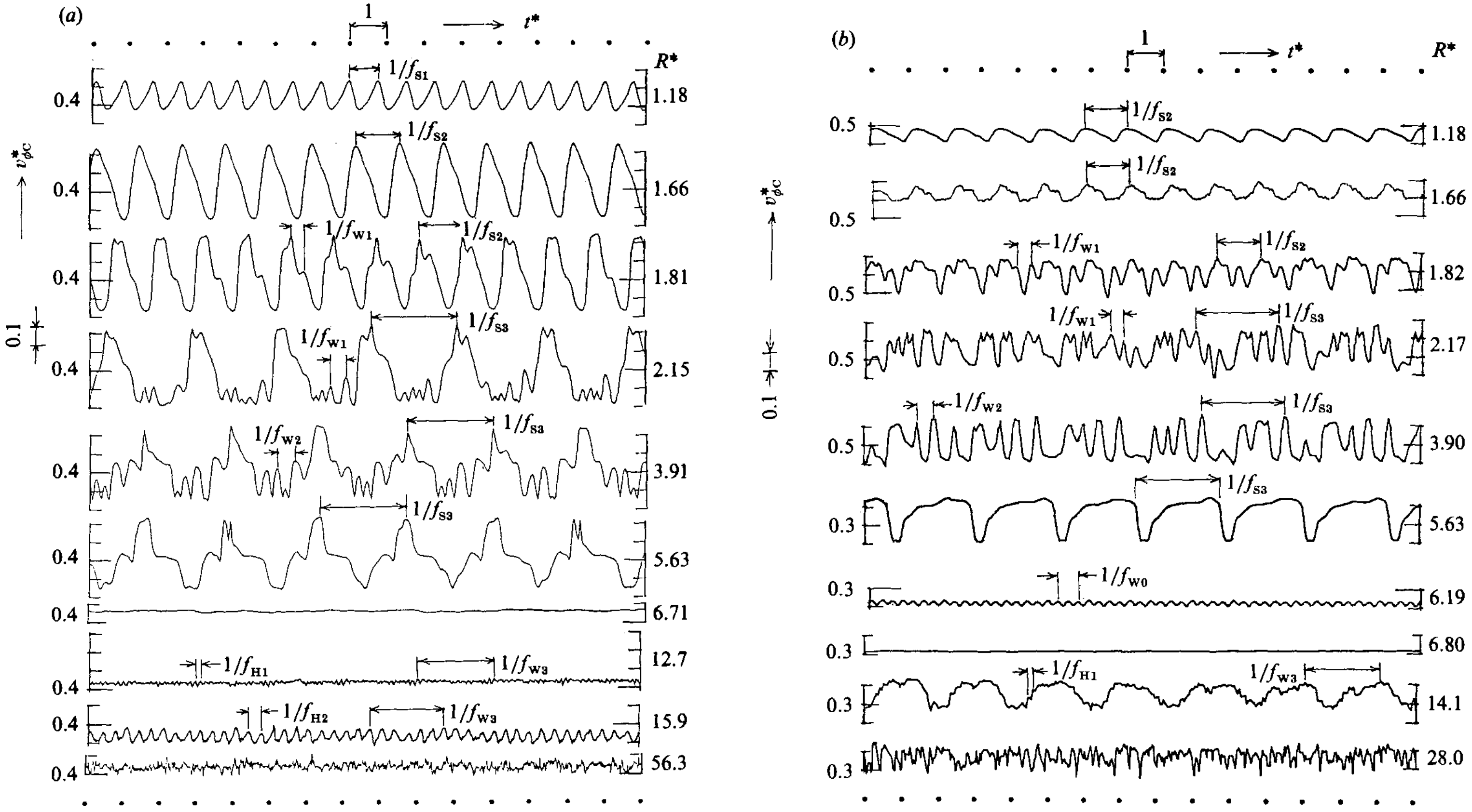

FIGURE 7. Temporal dependence and the fundamental periods of the azimuthal velocity components in the centre of the clearance at the colatitudes $\theta = 80°$ and $90°$. (*a*) $\theta = 80°$. (*b*) $\theta = 90°$.

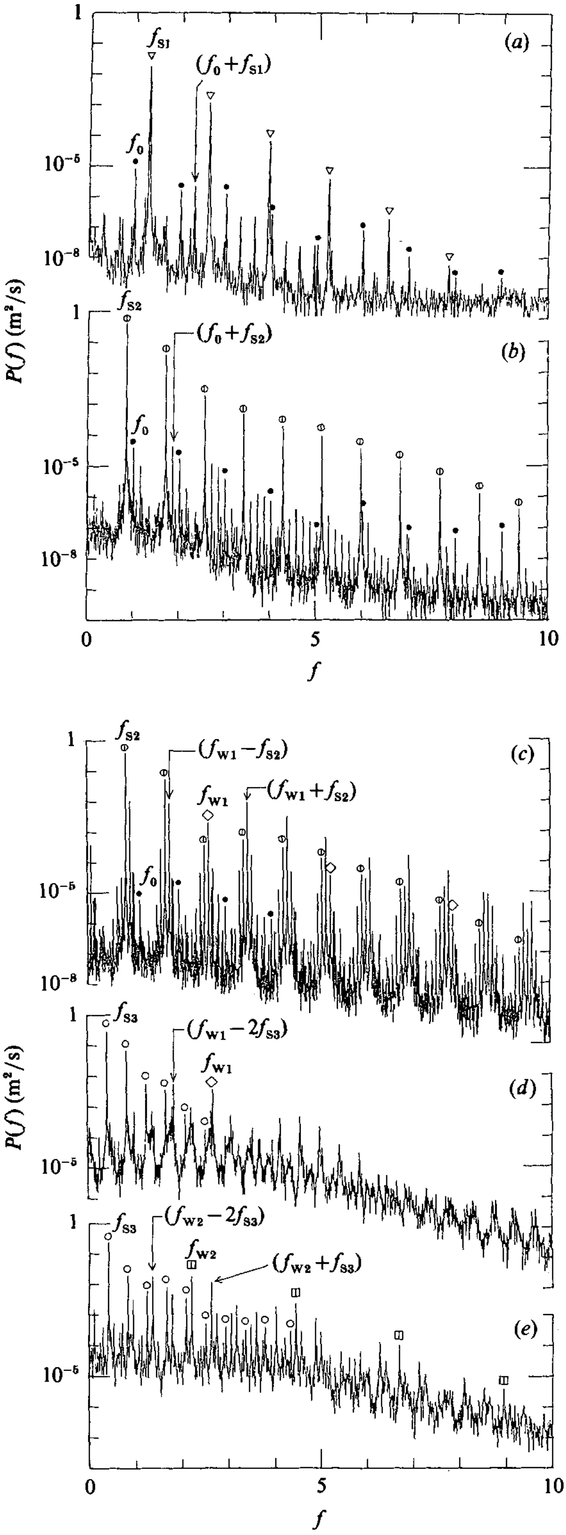

FIGURE 8. For caption see facing page.

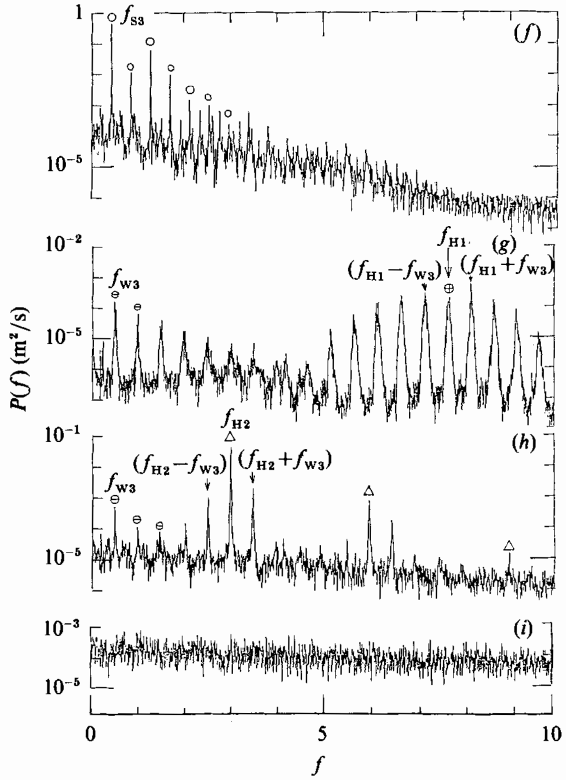

FIGURE 8. Power spectra of the velocity fluctuations in figure 7(*a*). The symbols ∇, ⦶, ○, ◇, ⊞, ⊖, ⊕ and △ indicate the fundamental frequency components $f_{S1}, f_{S2}, f_{S3}, f_{W1}, f_{W2}, f_{W3}, f_{H1}$ and f_{H2} (including their harmonics), respectively. The frequency components of f_0 and its harmonics, indicated by ●, are the instrumental artifacts. (*a*) $R^* = 1.18$. (*b*) $R^* = 1.66$. (*c*) $R^* = 1.81$. (*d*) $R^* = 2.15$. (*e*) $R^* = 3.91$. (*f*) $R^* = 5.63$. (*g*) $R^* = 12.7$. (*h*) $R^* = 15.9$. (*i*) $R^* = 56.3$.

corresponds to the spiral TG vortices with three pairs of vortex cells ($S_P = 3$) passing an observation point in the laboratory as described in §4.1. Another sharp frequency component labelled f_0 ($=1$), which equals the rotation frequency of the inner sphere, was caused by the whip of the rotating inner sphere. However, the intensity of f_0 is negligibly small in comparison with that of f_{S1}, so its effect cannot be suspected to influence the transition phenomena.

At $R^* = 1.66$, the spectrum contains a new single sharp frequency component labelled f_{S2}, which corresponds to the spiral TG vortices with two pairs of vortex cells ($S_P = 2$). The relations between frequency components and kinds of vortices or waves are discussed in §4.1 in detail. At $R^* = 1.81$, the spectrum contains the component f_{S2}, a new sharp frequency component labelled f_{W1}, their harmonics and many frequency components of their integer-linear combinations such as $C_1 f_{W1} + C_2 f_{S2}$ resulting from the nonlinear interaction between them, where C_1 and C_2 are integers. The frequency component f_{W1} corresponds to six travelling azimuthal waves ($m = 6$) passing the point of observation. For the case with plural fundamental frequency components of velocity fluctuation (e.g. f_{W1} and f_{S2} at $R^* = 1.81$), it is generally impossible to identify the fundamental frequencies only by means of the spectral analysis. In the present study, the fundamental frequencies are identified from the

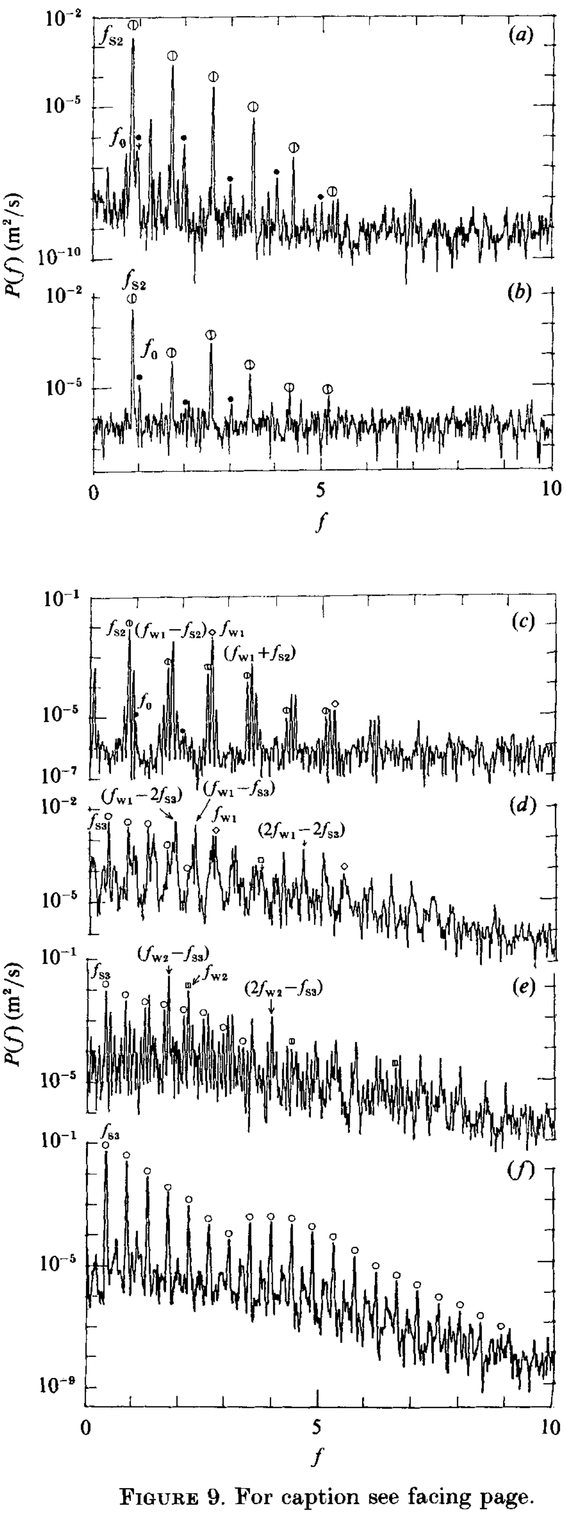

FIGURE 9. For caption see facing page.

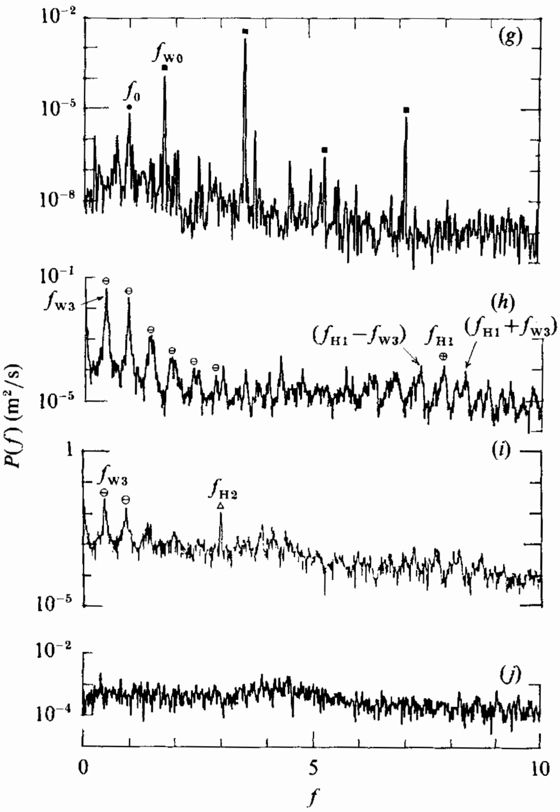

FIGURE 9. Power spectra of the velocity fluctuations in figure 7 (*b*). The symbols ⦶, ○, ◇, ◫, ⊖, ⊕, △ and ■ indicate the fundamental frequency components f_{S2}, f_{S3}, f_{W1}, f_{W2}, f_{W3}, f_{H1}, f_{H2} and f_{W0} (including their harmonics), respectively. The frequency components of f_0 and its harmonics, indicated by ●, are the instrumental artifacts. (*a*) $R^* = 1.18$. (*b*) $R^* = 1.66$. (*c*) $R^* = 1.82$. (*d*) $R^* = 2.17$. (*e*) $R^* = 3.90$. (*f*) $R^* = 5.63$. (*g*) $R^* = 6.19$. (*h*) $R^* = 14.1$. (*i*) $R^* = 15.9$. (*j*) $R^* = 28.0$.

comparison of velocity power spectra with both the visualization and the simultaneous laser measurements, as described in §4.1.

At $R^* = 2.15$, a new sharp frequency component labelled f_{S3} replaces the component f_{S2}, and the background continuum level increases to about 10^{-5} m^2/s. The component f_{S3} corresponds to the spiral TG vortices with a pair of vortex cells ($S_P = 1$). At $R^* = 3.91$, a new sharp frequency component labelled f_{W2}, which corresponds to five travelling azimuthal waves ($m = 5$), replaces the component f_{W1}. At $R^* = 5.63$, where the component f_{W2} disappears, the spectrum contains only the component f_{S3} and its harmonics. The disappearance of f_{W2} corresponds to the disappearance of the travelling azimuthal waves in the flow visualization. In the range $6.10 \leqslant R^* < 10.5$, since no velocity fluctuation appears as previously described, the power spectrum becomes zero. At $R^* = 12.7$, new broadband frequency components labelled f_{W3} and f_{H1} appear in the spectrum. They correspond to a travelling azimuthal wave ($m = 1$) and fourteen shear waves ($S_H = 14$), respectively. At $R^* = 15.9$, a new broadband frequency component labelled f_{H2}, which corresponds to around six shear waves ($S_H \approx 6$), appears in the spectrum. With an increase of R^*, the intensities of the components at f_{W3} and f_{H2} decrease,

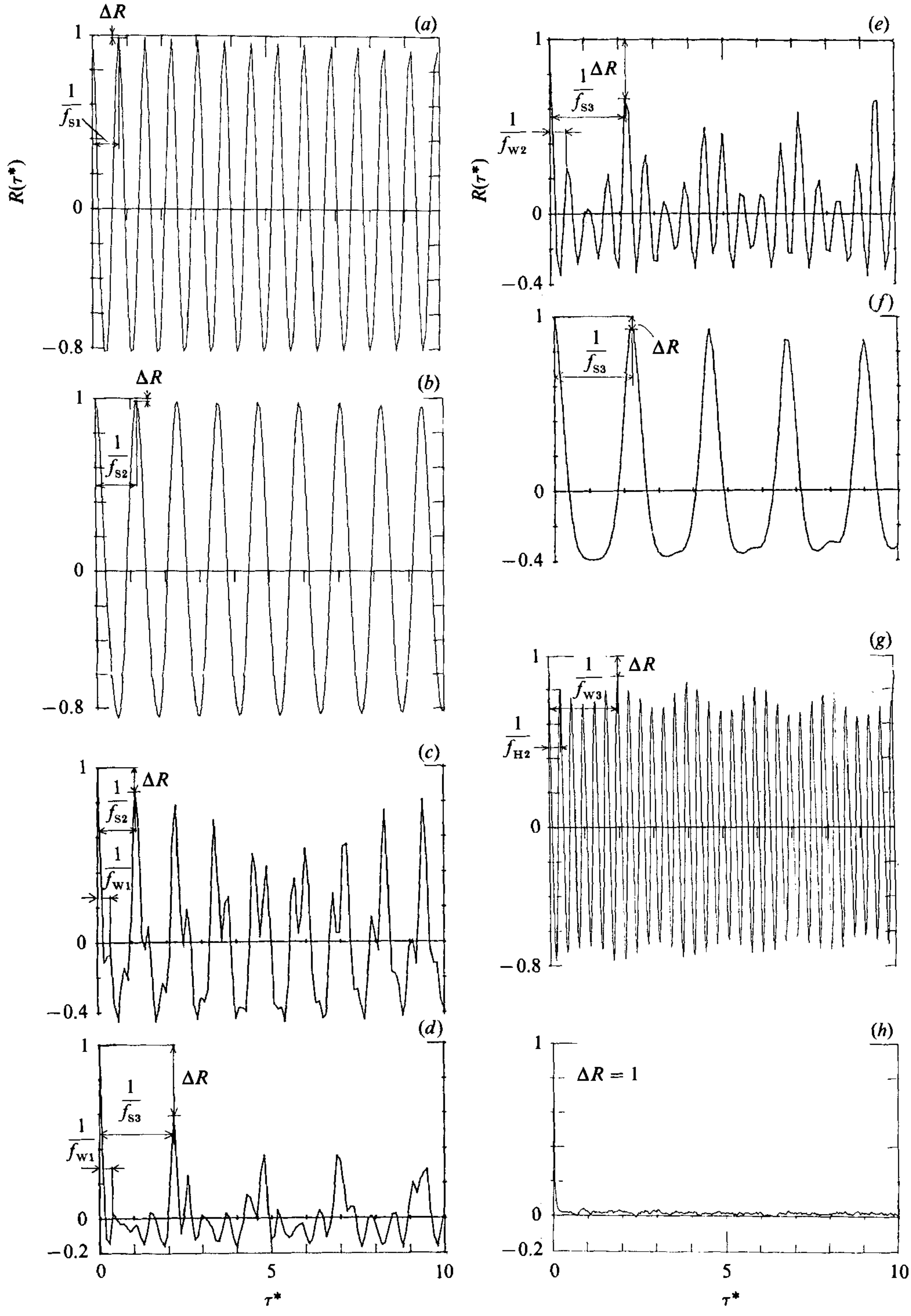

FIGURE 10. Autocorrelation coefficients of velocity fluctuations in the centre of the clearance at the colatitudes $\theta = 80°$ or $90°$. The variable ΔR is the decay of the autocorrelation coefficient, and $1/f_{S1}$, $1/f_{S2}$, etc., are the fundamental periods of the velocity fluctuations. (*a*) $R^* = 1.18$, $\theta = 80°$. (*b*) $R^* = 1.66$, $\theta = 80°$. (*c*) $R^* = 1.82$, $\theta = 90°$. (*d*) $R^* = 2.17$, $\theta = 90°$. (*e*) $R^* = 3.90$, $\theta = 90°$. (*f*) $R^* = 5.63$, $\theta = 90°$. (*g*) $R^* = 15.9$, $\theta = 80°$. (*h*) $R^* = 56.3$, $\theta = 80°$.

while the background continuum level increases, and consequently the continuous spectrum is presented, as shown at $R^* = 56.3$.

The power spectra of the velocity fluctuations at $\theta = 90°$ are shown in figure 9. The spectral evolution at $\theta = 90°$ is almost the same as that at $\theta = 80°$. But the sharp frequency components labelled f_{S2} and f_{W0} appear in the spectra for $R^* = 1.18$ and 6.19, respectively, which are undetected for the same R^* at $\theta = 80°$. This will be discussed in §4.2.

The autocorrelation coefficients $R(\tau^*)$ of velocity fluctuations are shown in figure 10(*a–h*). The abscissa τ^* in the same figure is a non-dimensional time lag which is stated in units of $1/f_0$. The $\Delta R(f)$ is defined as $1 - R(1/f)$ and describes the degree of randomness of the velocity fluctuation, as mentioned in §5. $1/f_{S1}$, $1/f_{S2}$, $1/f_{S3}$ and $1/f_{W3}$ are the delay times at which stronger autocorrelations appear (see figure 10). Figures 10(*a*) and 10(*b*) show almost cosine-type autocorrelations with the periods of $1/f_{S1}$ and $1/f_{S2}$, respectively, which indicates that the velocity fluctuations are almost sinusoidal. Figures 10(*c*)–10(*e*) show a strong autocorrelation with the period of $1/f_{S2}$ or $1/f_{S3}$ and a weak one with the period of $1/f_{W1}$ or $1/f_{W2}$. Thus, the autocorrelation related to the spiral TG vortices is stronger than that related to the travelling azimuthal waves, so $\Delta R(f) = \Delta R(f_S)$. Figure 10(*f*) indicates the strong periodic autocorrelation with the period of $1/f_{S3}$. Figure 10(*g*) shows the strong periodic autocorrelation with the period of $1/f_{W3}$ and the slightly weaker one with the period of $1/f_{H2}$. Accordingly, the autocorrelation related to the travelling azimuthal waves is usually stronger than that related to the shear waves, so $\Delta R(f) = \Delta R(f_{W3})$. Figure 10(*h*) shows the autocorrelation of a turbulent flow.

4. Fundamental frequencies

4.1. *Identification of fundamental frequencies*

The power spectra $P_L(f)$ of the scattered laser-light intensity at $\theta = 80°$ and $\eta = 0.5$ are shown in figure 11(*a–f*). The frequency component labelled f_0 as well as that in the velocity fluctuation power spectra was caused by the whip of the rotating inner sphere, as previously described. From the flow visualizations and the simultaneous spectral measurements by the scattered laser-light, the sharp frequency component f_{S1} in figure 11(*a*) was found to correspond to the spiral TG vortices with three pairs of vortex cells ($S_P = 3$, figure 4*a*) passing the observation point in the laboratory. In addition to this visual and spectral identification, the agreement of the value of f_{S1} in figure 11(*a*) with that in figure 8(*a*) (the velocity fluctuation power spectrum) shows definitely that f_{S1} is the fundamental frequency component of the spiral TG vortices of $S_P = 3$.

From a similar consideration, the sharp frequency components f_{S2} and f_{S3} in figures 8 and 11 are identified as the fundamental frequency components of the spiral TG vortices of $S_P = 2$ and 1, respectively. By the same flow visualization technique, the simultaneous spectral measurements and the agreement of frequency components of f_{W1} between figures 11(*c*) and 8(*d*), f_{W1} was found to be the fundamental frequency component of six travelling azimuthal waves ($m = 6$) passing the observation point.

Similarly, it is concluded that the frequency components f_{W2} and f_{W3} in figures 8 and 11 are the fundamental frequency components of the travelling azimuthal waves of $m = 5$ and 1, respectively. And it is also concluded that the frequency components f_{H1} and f_{H2} in figures 8 and 11 are the fundamental frequency components of fourteen

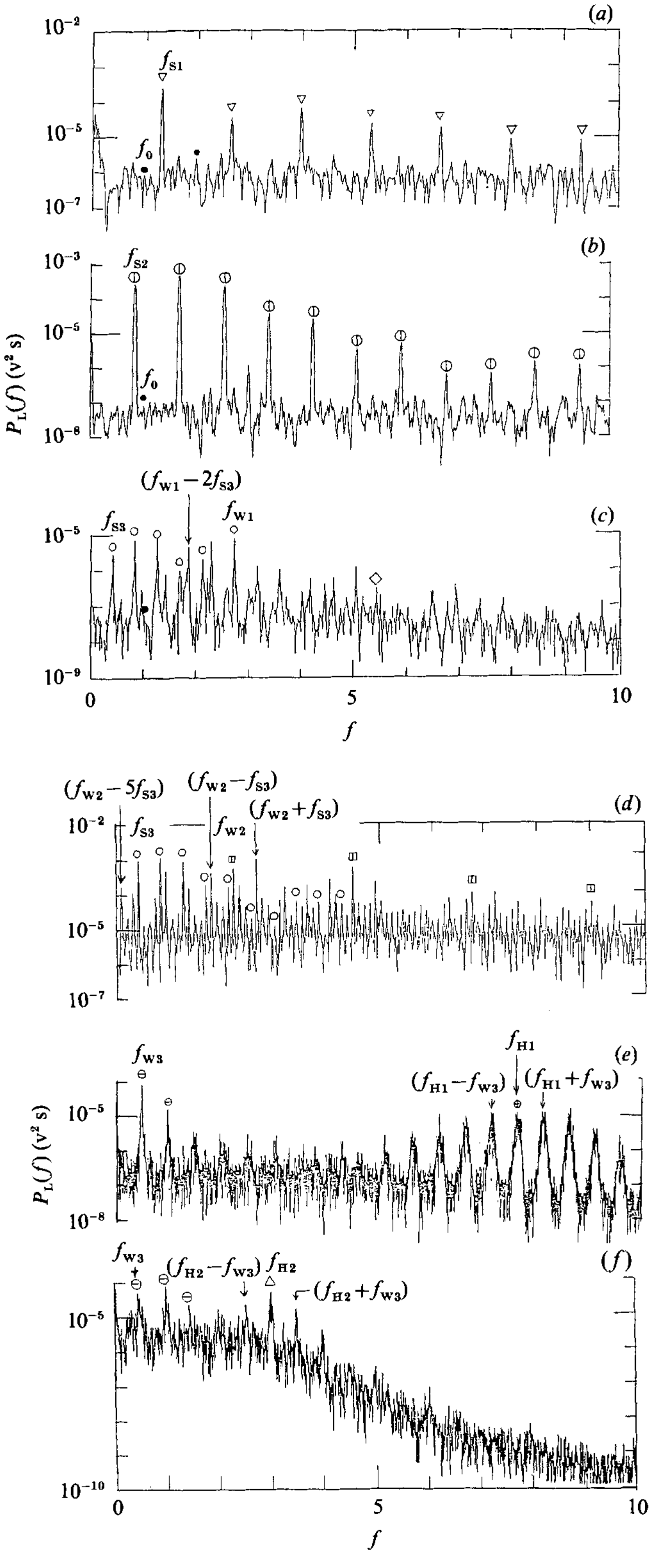

FIGURE 11. For caption see facing page.

shear waves ($S_H = 14$, figure 4*c*) and about six shear waves ($S_H \approx 6$, figure 4*d*) passing the observation point, respectively.

The frequency components $f_{S2}, f_{S3}, f_{W1}, f_{W2}, f_{W3}, f_{H1}$ and f_{H2} at $\theta = 90°$ in figure 9 were also found to be the same fundamental frequency components as those at $\theta = 80°$ from the same consideration as described above.

The types of the fundamental frequencies found in the present experiment are summarized as follows. The three kinds of fundamental frequencies, f_S, f_W and f_H, correspond to the spiral TG vortices, the travelling azimuthal waves on the toroidal TG vortices and the shear waves within the secondary flow, respectively. The schematics of the flows in typical flow regimes and these fundamental frequencies are shown in figure 12.

4.2. *Spatial characteristics and evolution of fundamental frequency components*

The relationship between the fundamental frequency components expressed by their wavenumbers and the colatitude is shown in figure 13. The fundamental frequency components could be detected not only over the θ-ranges shown by solid lines, where the corresponding disturbances such as the spiral TG vortices, the travelling azimuthal waves and the shear waves were clearly observed (figure 5*b*), but also over the θ-ranges indicated by broken lines, where they were not clearly observed. The values of the fundamental frequency components are constant independently of θ. The power spectra of the velocity fluctuations measured by the hot-wire anemometer at $\eta = 0.1$, 0.5 and 0.9 are shown in figure 14(*a–c*), respectively. Although the peak values of power at f_{W3} and f_{H2} depend on η, the values of f_{W3} and f_{H2} are independent of η. Thus, it is known that the values of fundamental frequency components are independent of both θ and η.

The relationship between the fundamental frequency components and R^* is shown in figure 15, compared with that in the circular Couette flow. An indication ○ shows the values of the fundamental frequency obtained by the spectral analysis of the scattered light intensity, while ×, + and ◓ indicate those obtained from the velocity fluctuation spectra. The × indication shows the data in which there is complete agreement between the frequency values at $\theta = 80°$ and 90°. The symbols + (f_{S1}) at $\theta = 80°$ and ◓ (f_{S2} and f_{W0}) at $\theta = 90°$ show discrepancy. On the other hand, the data (○) obtained by the scattered light intensity agree well with those obtained by the velocity fluctuation except for f_{S2} (◓) for $R^* \approx 1.2$ and f_{W0} for $R^* \approx 6.2$.

In order to investigate the discrepancy which can be seen in f_{S2} for $R^* \approx 1.2$ and in f_{W0} for $R^* \approx 6.2$, the following additional experiments were pursued by means of the simultaneous spectral and flow-visualization measurements. First of all, the Reynolds number was increased from zero to $R^* = 1.18$ with some acceleration, but not quasi-statically. The flow regime of II TS$_N$($N = 2$, $S_P = 2$) and the fundamental frequency component f_{S2} were obtained, but not f_{S1}, as shown in figure 16(*a*). Next,

FIGURE 11. Power spectra of the scattered laser-light intensity in the centre of the clearance at the colatitude $\theta = 80°$. The symbols ▽, ⦶, ○, ◇, ◫, ⊖, ⊕ and △ indicate the fundamental frequency components $f_{S1}, f_{S2}, f_{S3}, f_{W1}, f_{W2}, f_{W3}, f_{H1}$ and f_{H2} (including their harmonics), respectively. The components of f_0 and its harmonics, indicated by ●, are the instrumental artifacts. (*a*) f_{S1} in II TS$_N$ ($N = 2$, $S_P = 3$) at $R^* = 1.18$. (*b*) f_{S2} in II TS$_N$ ($N = 2$, $S_P = 2$) at $R^* = 1.66$. (*c*) f_{S3} and f_{W1} in III WTS$_N$ ($N = 2$, $S_P = 1$, $m = 6$) at $R^* = 2.15$. (*d*) f_{S3} and f_{W2} in III WTS$_N$ ($N = 2$, $S_P = 1$, $m = 5$) at $R^* = 3.91$. (*e*) f_{W3} and f_{H1} in IV WTS$_h$ ($N = 2$, $m = 1$, $S_H = 14$) at $R^* = 12.7$. (*f*) f_{W3} and f_{H2} in IV WTS$_h$ ($N = 2$, $m = 1$, $S_H \approx 6$) at $R^* = 15.9$.

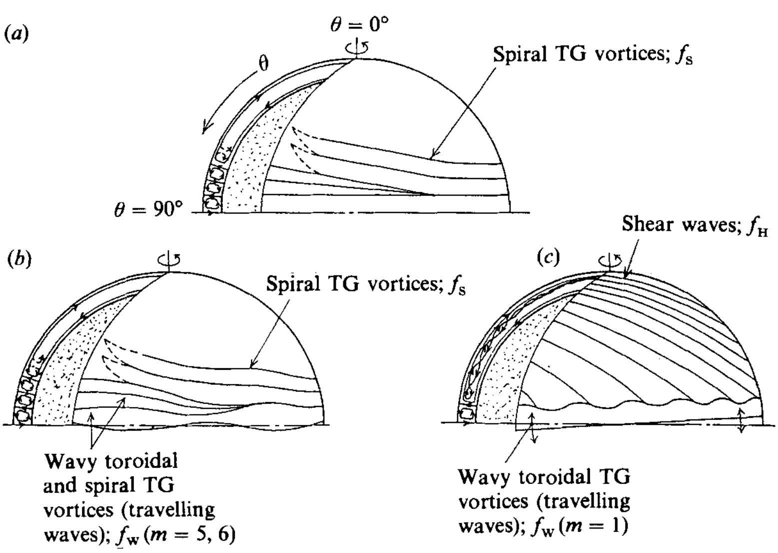

FIGURE 12. Schematics of the flows in typical flow regimes and the three fundamental frequency components f_S, f_W and f_H. (a) II TS or III TS with f_S. (b) III WTS with f_S and f_W. (c) IV WTS$_h$ with f_W and f_H.

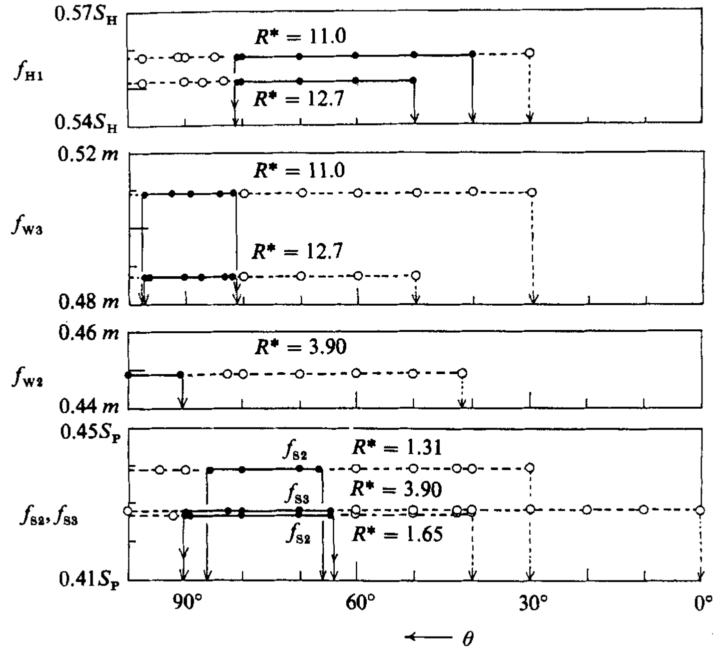

FIGURE 13. Relationship between the fundamental frequency components expressed by their wavenumbers and the colatitude, obtained by the power spectra of the scattered laser-light intensity in the centre of the clearance. The solid lines conjoining solid circles (experimental result) indicate the meridian ranges, where the corresponding disturbances such as the spiral TG vortices, the travelling azimuthal waves and the shear waves were clearly observed. The broken lines conjoining empty circles (experimental result) indicate the meridian ranges, where they were not clearly observed.

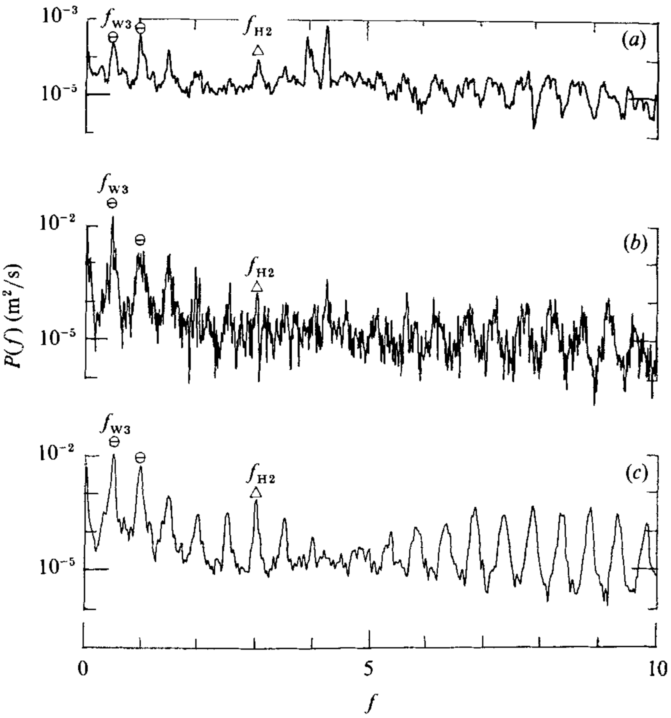

FIGURE 14. Power spectra of the velocity fluctuations measured by the hot-wire anemometer at $\eta = 0.1$, 0.5 and 0.9 at the equator for the flow of the regime IV WTS$_h$ ($N = 2$, $m = 1$, $S_h \approx 6$) at $R^* = 15.1$. (*a*) $\eta = 0.1$. (*b*) $\eta = 0.5$. (*c*) $\eta = 0.9$.

the R^* was similarly increased from zero to $R^* = 6.19$, then the flow regime III WT($N = 2$, $m = 4$) and $f_W(m = 4)$ ($=f_{W0}$) were obtained, as shown in figure 16(*b*). From these results we understand that the discrepancy at $R^* \approx 1.2$ comes from the difference of flow states between $S_P = 2$ and $S_P = 3$, which was caused by the fact that the wake behind the hot-wire prong located at $\theta = 90°$ is not so negligibly small as that at $\theta = 80°$ for $R^* \approx 1.2$. The discrepancy at $R^* \approx 6.2$ also comes from the similar difference of flow regimes between III WT and III T. However, no discrepancy can be seen over the other range of R^*. Hence, the data of hot-wire measurements are assured as well as those of simultaneous spectral and flow-visualization measurements without the wake, except for those of hot-wire measurement at $\theta = 90°$ for $R^* \approx 1.2$ and 6.2.

The fundamental frequencies f_S, f_H and f_W which are confirmed as mentioned above, are summarized in table 2. The flow regimes of II TS$_N$ and III TS$_N$ are singly periodic regimes characterized by a single-frequency component (f_S), while the flow regimes of III WTS$_N$ and IV WTS$_h$ are doubly periodic regimes characterized by two fundamental frequency components $[f_S, f_W]$ and $[f_W, f_H]$, respectively. In the ranges $R^*_4 \leqslant R^* < R^*_{5a}$ and $R^*_6 \leqslant R^* \leqslant R^*_{\max}$, no fundamental frequency components could be detected, i.e. in the former range the velocity fluctuation disappeared (the relaminarizing flow occurs), whereas in the latter range it became chaotic.

On the other hand, Bühler & Zierep (1984) obtained two fundamental frequency components ν_1 and ν_2 in the TG vortex flow with two toroidal cells for $\beta = 0.177$, as shown in figure 15. ν_1 is the fundamental frequency component of the shear waves

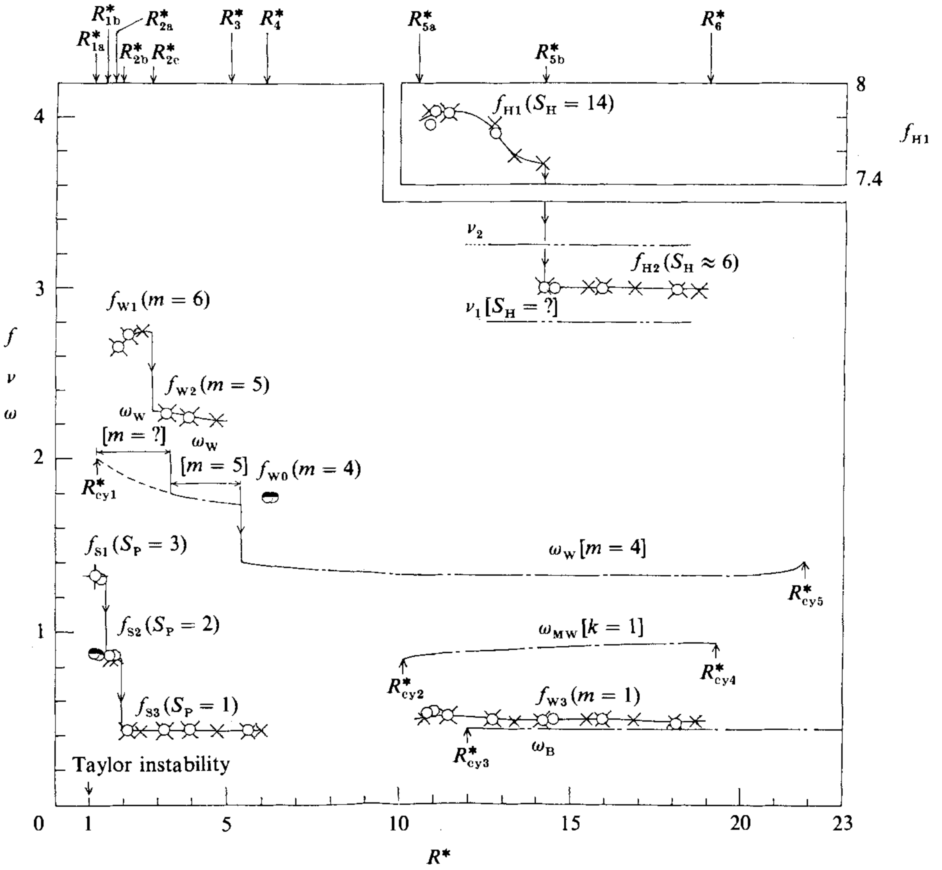

FIGURE 15. Reynolds-number dependences of the fundamental frequency components of the velocity fluctuations: ○, present data obtained from the power spectra of the scattered light intensity; ×, present data obtained from the velocity fluctuation power spectra both at the colatitudes $\theta = 80°$ and $90°$; +, present data obtained from the velocity fluctuation power spectra at $\theta = 80°$; ●, present data obtained from the velocity fluctuation power spectra at $\theta = 90°$. ----, ν_1 and ν_2, data for $\beta = 0.177$ obtained by Bühler & Zierep (1984); ---, ω_W, ω_{MW} and ω_B, data, and $R^*_{cy1} = 1.2$, $R^*_{cy2} = 10.1$, $R^*_{cy3} = 12$, $R^*_{cy4} = 19.3$, $R^*_{cy5} = 21.9$, transition Reynolds numbers for the regime transition, respectively, obtained in the circular Couette flow for $\beta = 0.14$ and $\Gamma = 20.0$ by Fenstermacher *et al.* (1979).

within the secondary flow, although their wavenumber has not been reported. The value of ν_1 is much smaller than that of f_{H1}. The physical characteristic of ν_2 is not described in detail. Although ν_2 is considered a fundamental frequency of a secondary instability established within the Taylor vortices in their paper, the value of ν_2 is very different from the present f_{W3}, being rather near the value of f_{H2}.

The Reynolds number dependences of the rotation frequencies of the spiral TG vortices, the travelling azimuthal waves and the shear waves, f_S/S_P, f_W/m and f_H/S_H, are shown in figure 17. The values of f_S/S_P, f_W/m and f_H/S_H are nearly constant as the Reynolds number is increased, and differ slightly from one another.

As for the rotation frequency f_W/m in the spherical Couette flow, the clearance ratio dependence of f_W/m is shown in figure 18. The range of uncertainty means the

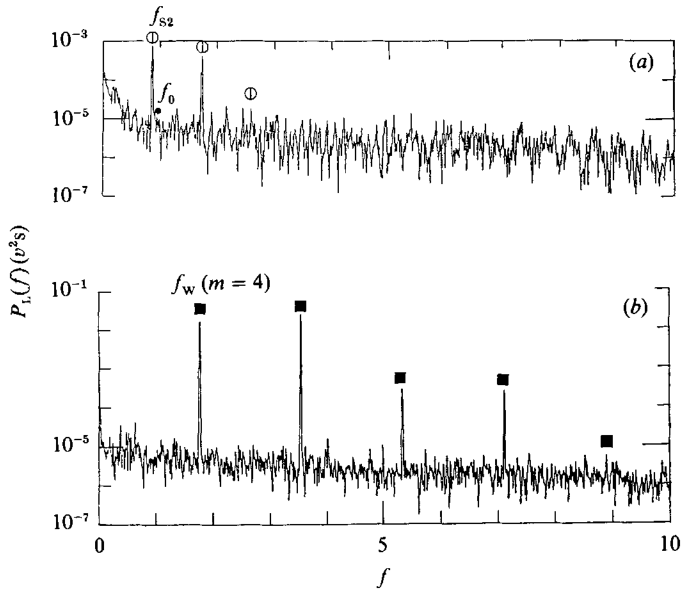

FIGURE 16. Scattered light intensity spectra in the centre of the clearance at the equator under the condition that the Reynolds number was increased with some acceleration rate. (a) f_{S2} in IITS_N ($N = 2$, $S_P = 2$) at $R^* = 1.18$. The ⦶ indicates the fundamental frequency component f_{S2} and its harmonics. The frequency component f_0 indicated by ● is an instrumental artifact. (b) f_W ($m = 4$) in IIIWT ($N = 2$, $m = 4$) at $R^* = 6.19$. ■ indicates the fundamental frequency component f_W ($m = 4$) and its harmonics.

range between the maximum and minimum values in the relationship between f_W/m and R^* as shown in figure 17. The Taylor instability occurs in the present data for $\beta = 0.14$, but not in those of Yavorskaya *et al.* (1980) for $\beta = 0.398$–1.33, as described previously. The present data, however, seem to be on the extrapolated curve of those of Yavorskaya *et al.*

4.3. *Comparison with circular Couette flow*

Toroidal TG vortices near the equator in the spherical Couette system are similar to Taylor vortices in the circular Couette system, but the former is influenced by the Ekman boundary layer. Therefore, it is interesting in the consideration of the Ekman boundary-layer effect on the toroidal TG vortices to discuss the fundamental frequencies and the transition Reynolds numbers, comparing both the spherical and circular Couette systems.

In figure 15, R^*_{cy1}–R^*_{cy5} are the transition Reynolds numbers for regime transition, and ω_W, ω_{MW} and ω_B are the characteristic frequency components which were obtained in the circular Couette flow for the aspect ratio $\Gamma = 20.0$ and $\beta = 0.14$ by Fenstermacher *et al.* (1979). ω_W and ω_B are the fundamental frequency component of the travelling azimuthal waves and the broad component of a weak turbulence, respectively. Gorman & Swinney (1982) found that ω_{MW} is the frequency component of the modulated travelling azimuthal waves. Since the value of transition Reynolds number for the onset of the travelling azimuthal waves in the spherical Couette flow ($R^*_{2a} = 1.71$) is greater than in the circular Couette flow ($R^*_{cy1} = 1.2$), the Ekman boundary-layer effect in the spherical Couette flow acts on the stable side for the

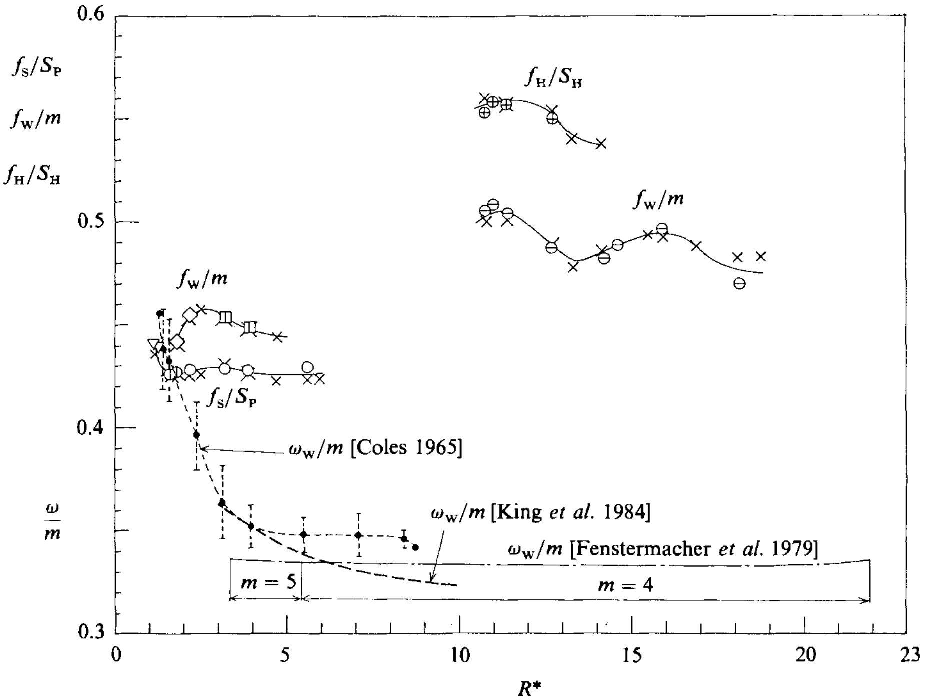

FIGURE 17. Reynolds-number dependences of the rotation frequencies of the spiral TG vortices, the travelling azimuthal waves and the shear waves: ▽, $f_{S1}/3$; ⊖, $f_{S2}/2$; ○, $f_{S3}/1$; ◇, $f_{W1}/6$; ◫, $f_{W2}/5$; ⊖, $f_{W3}/1$; ⊕, $f_{H1}/14$ present data obtained from the power spectra of the scattered light intensity; ×, present data obtained from the velocity spectra at the colatitudes $\theta = 80°$ and $90°$. The data of ω_W/m in the circular Couette flow: – - –, $\beta = 0.140$, $\Gamma = 20.0$ (aspect ratio), $m = 4, 5$ (Fenstermacher *et al.* 1979); ——, $\beta = 0.152$, $\Gamma_{max} = 80$ (the largest aspect ratio), $m = 4, 5$ (King *et al.* 1984); ------, $\beta = 0.144$, $\Gamma = 27.9$, $m = 3$–7 (Coles 1965).

onset of the travelling azimuthal waves. As the Reynolds number is increased from $R^* \approx 3$, the wavenumber changes to $m = 5$, $m = 0$ (travelling wave disappears) and $m = 1$ by turns in the spherical Couette flow. But in circular Couette flow, five waves, four waves, four waves with the modulation and four waves appear by turns. The temporary disappearance of the travelling waves and no modulation are characteristic of the travelling azimuthal waves in the spherical Couette flow.

The rotation frequencies ω_W/m of the travelling azimuthal waves, as shown in figure 17, are for relatively large aspect ratios and approximately the same clearance ratios as the present one ($\beta = 0.14$) in the circular Couette flow. Although the values of ω_W/m decrease monotonically with increasing R^* until they reach their plateaux, the rotation frequency f_W/m in the spherical Couette flow does not decrease and are much greater than ω_W/m for the higher range in R^*.

On the other hand, the ranges of maximum and minimum values of ω_W/m over the all R^* range in the circular Couette flow of $\Gamma_{max} = 26$–115 and $\beta = 0.0526$–0.588, obtained by King *et al.* (1984), are shown in figure 18. The rotation frequency in the spherical Couette flow (f_W/m) shows the same tendency as ω_W/m in the circular Couette flow, but the former is greater than the latter throughout the range of β. King *et al.* (1984) demonstrated that ω_W/m has the tendency of monotonic increase as a decrease of aspect ratio Γ. From the above-mentioned relation between ω_W/m

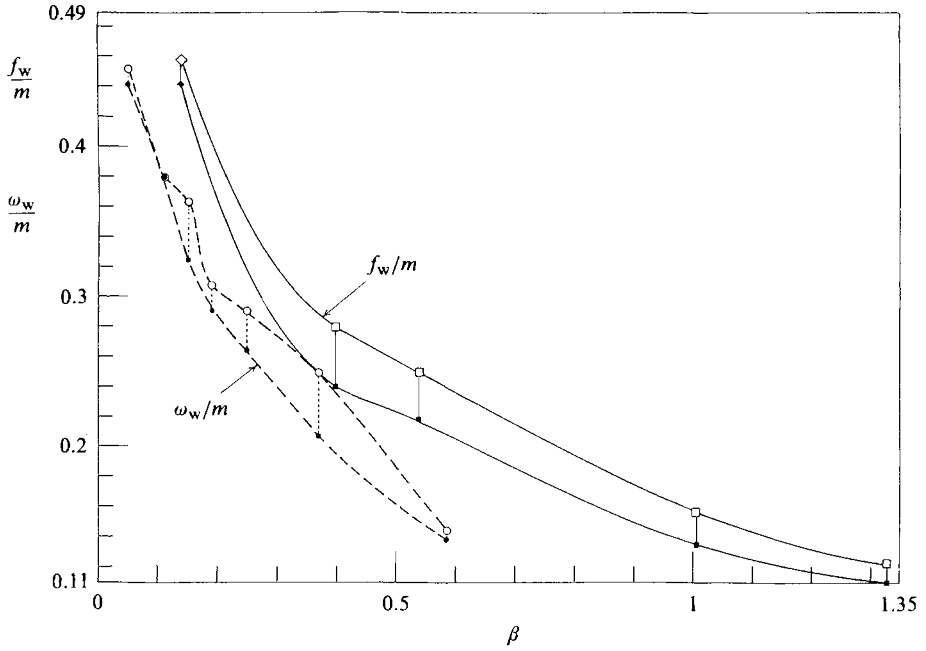

FIGURE 18. Clearance-ratio dependence of the rotation frequency of the travelling azimuthal waves. The range of uncertainty means the range between the maximum and minimum values in the relationship between f_W/m and R^* or between ω_W/m and R^*: ◇ (maximum) and ◆ (minimum), present data for $\beta = 0.14$; □ (maximum) and ■ (minimum), data for $\beta = 0.398$–1.33 of Yavorskaya *et al.* (1980) in the spherical Couette flow; ○ (maximum and ● (minimum), data for $\beta = 0.0526$–0.588 and $\Gamma_{max} = 26$–115 of King *et al.* (1984) in the circular Couette flow.

and Γ, the end effect of the cylinders is known to increase ω_W/m in the circular Couette flow. Since the end effect in the circular Couette flow corresponds to the Ekman boundary-layer effect in the spherical Couette flow, the Ekman boundary-layer effect is presumed to increase f_W/m in the spherical Couette flow.

Remarkable characteristics of the spherical Couette flow are described as follows. As mentioned previously, neither the modulation of the travelling azimuthal waves such as ω_{MW} nor the weak turbulence such as ω_B could be detected in the present spherical Couette flow measurements, where the Reynolds number was quasi-statically increased from zero. However, under the condition that the Reynolds number is increased with a given acceleration, the modulation of the travelling azimuthal waves appears as will be reported in our next paper. And the fundamental frequencies f_S and f_H are characteristic only of the spherical Couette flow.

5. Development of turbulence

Since a velocity fluctuation autocorrelation coefficient approaches an uncorrelated one as the chaotic element increases in a flow, Yavorskaya *et al.* (1980) defined the decay of the velocity fluctuation autocorrelation coefficient, $\Delta R(f) = 1 - R(1/f)$, as the quantitative value describing the degree of randomness of the velocity fluctuation in the spherical Couette flow. On the other hand, Sato & Saito (1975) defined a randomness factor z, the ratio of the energy contained in a background continuous

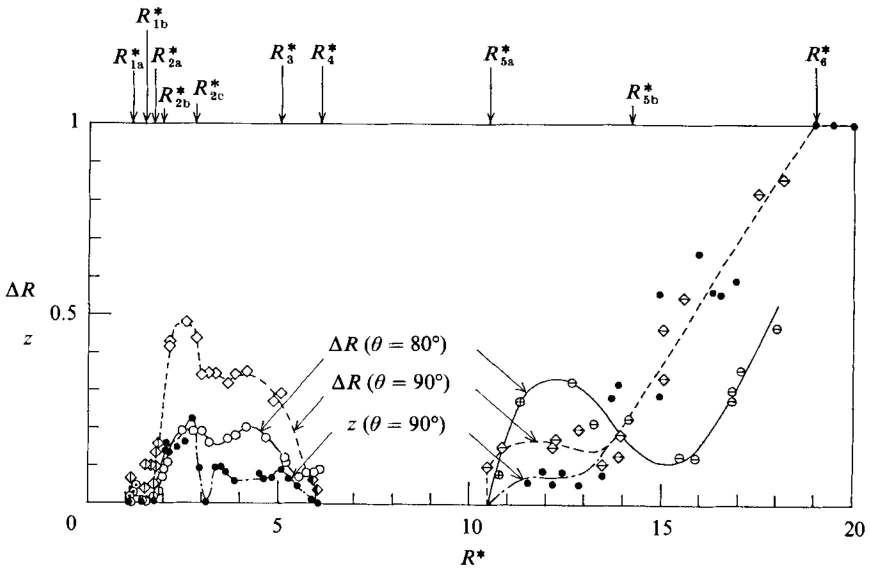

FIGURE 19. Growth in the degree of randomness in the velocity fluctuation, defined by the decay of the autocorrelation coefficient $\Delta R(f)$ and the randomness factor z, in the centre of the clearance at the colatitudes $\theta = 80°$ and $90°$. The symbols ⊙, ⦶, ○, ⊕ and ⊖ indicate the decay of the autocorrelation coefficient $\Delta R(f_{s1})$, $\Delta R(f_{s2})$, $\Delta R(f_{s3})$, $\Delta R(f_{H1})$ and $\Delta R(f_{w3})$ at $\theta = 80°$. The symbols ⟐, ◇, ⬗ and ⟠ indicate the decay of the autocorrelation coefficient $\Delta R(f_{s2})$, $\Delta R(f_{s3})$, $\Delta R(f_{w0}/3)$ and $\Delta R(f_{w3})$ at $\theta = 90°$. The symbol ● indicates z at $90°$.

spectrum ([total fluctuation energy] − [regular fluctuation energy contained in line and broadband spectral]) to the total fluctuation energy, for a two-dimensional wake. We also adopted the same definitions, $\Delta R(f)$ and z, as the values describing the degree of randomness of the velocity fluctuation.

The growth of the value of ΔR and z in the centre of the gap are shown at $\theta = 80°$ and $90°$ in figure 19. Below R^*_4, the curve of $\Delta R(\theta = 90°)$ shows a Reynolds-number dependence similar to that of $\Delta R(\theta = 80°)$ or $z(\theta = 90°)$, but the former is greater than the latter. And the value of z is smaller than that of ΔR. The values of $\Delta R(\theta = 80°$ and $90°)$ and $z(\theta = 90°)$ become zero in the range $R^*_4 \leqslant R^* < R^*_{5a}$, where the velocity fluctuation disappears and the flow returns to the time-independent toroidal TG vortex flow (the flow regime IIIT, table 2). Beyond R^*_{5a}, $z(\theta = 90°)$ increases in the same way as $\Delta R(\theta = 90°)$ with increasing R^*. However, $\Delta R(\theta = 80°)$ first increases earlier than $\Delta R(\theta = 90°)$, decreases in $12 \lesssim R^* \lesssim 15$ and then increases later than $\Delta R(\theta = 90°)$ with increasing R^*. Beyond R^*_{5b}, the chaos of the flow can be guessed to grow much more for $\theta = 90°$ than for $\theta = 80°$.

The non-dimensional turbulence intensities (r.m.s. values $\hat{v}^*_\phi = \hat{v}_\phi/(2\pi R_1 f_0)$) of the fluctuating azimuthal velocity component are shown in figure 20. Figure 20(*a*) gives the Reynolds number dependences of the turbulence intensities at $\eta = 0.5$, $\hat{v}^*_{\phi C} = \hat{v}^*_\phi(\eta = 0.5)$, for $\theta = 80°$ and $90°$. In the range $R^*_C \leqslant R^* < R^*_4$, the turbulence intensity at $\theta = 80°$ is greater than that at $\theta = 90°$, and the Reynolds number at which the turbulence intensity becomes maximum for $\theta = 80°$ is different from that for $\theta = 90°$. These Reynolds numbers for $\theta = 80°$ and $90°$ are not in agreement with the Reynolds number at which ΔR or z has the maximum value (cf. figures 19 and 20*a*). Accordingly, it is argued that the root-mean square value of the velocity

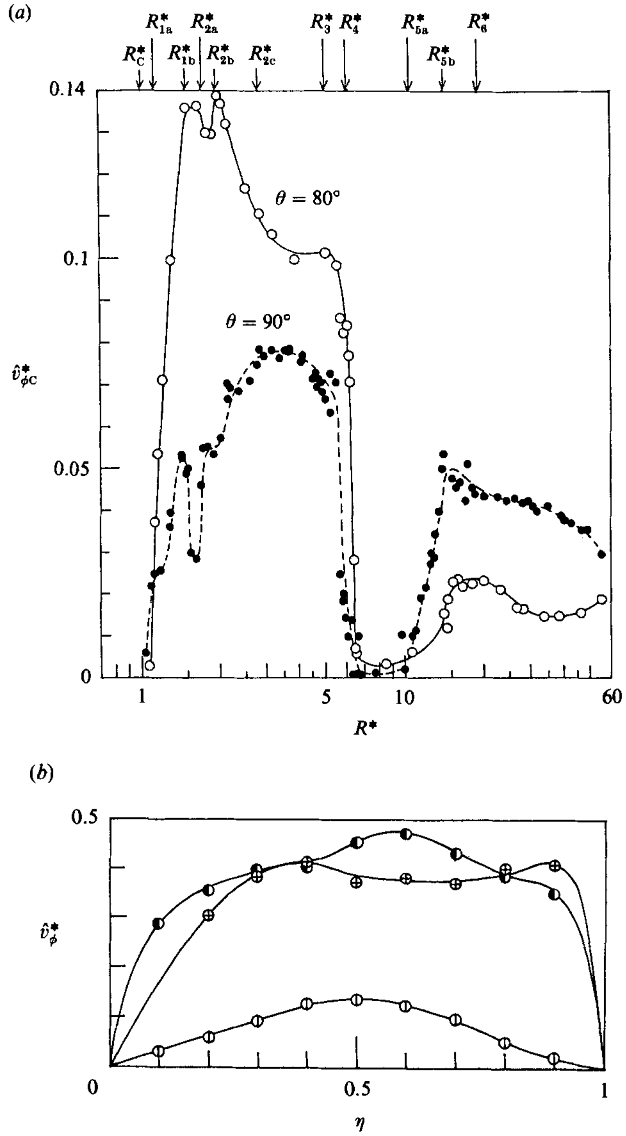

FIGURE 20. Relationship between the turbulence intensity of the fluctuating azimuthal velocity component and the Reynolds number. (*a*) Turbulence intensity in the centre of the clearance at colatitudes $\theta = 80°$ and $90°$: ○, $\theta = 80°$; ●, $\theta = 90°$. (*b*) Distribution in the clearance of the turbulence intensity at the equator: ⦶, $R^* = 1.19$; ⊕, $R^* = 15.1$; ◐, $R^* = 19.6$.

fluctuation corresponds directly with the degree of randomness of the flow, but rather that the energy of velocity fluctuation contains the greater part of energy as the regular periodic motion in the lower R^* value range.

In the range $R^*_4 \leqslant R^* < R^*_{5a}$, $\hat{v}^*_{\phi c}$ as well as ΔR and z becomes zero, because the relaminarization seems to occur, as described previously. Above R^*_{5a}, since the travelling azimuthal waves and the shear waves appear, both turbulence intensities $\hat{v}^*_{\phi c}$ for $\theta = 80°$ and $90°$ increase. But, beyond about R^*_{5b} they tend to decrease slightly with an increase of R^*. Figure 20(*b*) shows the distributions of the turbulence intensity $\hat{v}_\phi^*$ in the gap at $\theta = 90°$. The profile of $\hat{v}_\phi^*$ at $R^* = 1.19$, where the spiral TG vortices appear, is almost symmetric with respect to $\eta = 0.5$. But the profile at $R^* = 15.1$ is asymmetric with respect to $\eta = 0.5$. Since f_{W3} and f_{H2} are obtained for $\theta = 90°$ around $R^* = 14$–19, the reason why $\hat{v}_\phi^*$ becomes greater near the outer sphere would be that the shear waves influence the velocity fluctuation closer to the outer sphere than to the inner sphere, and that the chaos grows near the outer sphere. The profile at $R^* = 19.6$ approaches a symmetric profile with respect to $\eta = 0.5$, because the chaotic element increases in the flow with R^*.

6. Conclusions

We have considered the characteristics of the laminar–turbulent transition of the Taylor–Görtler (TG) vortex flow in the spherical Couette system. With increasing Reynolds number, the mean velocity profile in the gap is influenced by the location of both sink and source on the inner sphere, because of the momentum transfer depending on the inflow and outflow boundaries of the stationary vortices which can move with the Reynolds number. On the other hand, the fluctuating velocity corresponds to the periodic or unperiodic motions of vortices.

By velocity and simultaneous spectral and flow-visualization measurements, three kinds of fundamental frequencies, f_S, f_W and f_H, were found, which correspond to the spiral TG vortices, the travelling azimuthal waves on toroidal TG vortices and the shear waves within the Ekman boundary layer, respectively. The interaction between fundamental frequencies, e.g. wave interaction between the travelling waves and shear waves, cannot be observed by flow visualization, but can be detected by the scattered-light measurements and velocity measurements over a wider range of the meridian angle. Each fundamental frequency has a value completely independent of the meridian angle and wall distance from the inner sphere. Although each fundamental frequency has a discrete value depending on the wavenumber which varies with the Reynolds number, each rotation frequency (i.e. fundamental frequency scaled by the wavenumber) has a value almost independent of the Reynolds number. The rotation frequencies differ in terms of the spiral TG vortices, the travelling azimuthal waves and the shear waves. The spiral TG vortices and the shear waves are characteristic of the spherical Couette flow, although the travelling azimuthal wave is a common type of disturbance appearing in both the spherical and circular Couette flows. The components of the modulated waves (ω_{MW}) and the weak turbulence (ω_B) appearing in the circular Couette flow could not be detected in the present experiment. In spherical Couette flow, the preturbulent flow is also characterized by not more than two fundamental frequency components.

Another characteristic of the present transition is the occurrence of relaminarizing flow in $R_4^* \leqslant R^* < R_{5a}^*$, where the non-dimensional r.m.s. value of fluctuating velocity is almost zero, with increasing Reynolds number, after its first increase and the following decrease. The non-dimensional r.m.s. values of fluctuating velocity, the decay of the autocorrelation coefficient and the randomness factor also increase with the appearance of shear waves. However, the non-dimensional r.m.s. values of fluctuating velocity then gradually decrease with the development of the chaos in the flow.

REFERENCES

Bartels, F. 1982 Taylor vortices between two concentric rotating spheres. *J. Fluid Mech.* **119**, 1.

Belyaev, Yu. N., Monakhov, A. A., Scherbakov, S. A. & Yavorskaya, I. M. 1979 Onset of turbulence in rotating fluids. *J. Exp. Theor. Phys. Lett.* **29**, 329.

Belyaev, Yu. N., Monakhov, A. A., Scherbakov, S. A. & Yavorskaya, I. M. 1984 Some routes to turbulence in spherical Couette flow. In *Laminar–Turbulent Transition* (ed. V. V. Kozlov), p. 669. Springer.

Bouabdallah, A. & Cognet, G. 1980 Laminar-turbulent transition in Taylor–Couette flow. In *Laminar–Turbulent Transition* (ed. R. Eppler & H. Fasel), p. 368. Springer.

Bühler, K. & Zierep, J. 1983 Transition to turbulence in a spherical gap. *Proc. 4th Intl Symp. on Turbulent Shear Flows*. University of Karlsruhe.

Bühler, K. & Zierep, J. 1984 New secondary flow instabilities for high *Re*-number flow between two rotating spheres. In *Laminar–Turbulent Transition* (ed. V. V. Kozlov), p. 677. Springer.

Coles, D. 1965 Transition in circular Couette flow. *J. Fluid Mech.* **21**, 385.

Dennis, S. C. R. & Quartapelle, L. 1984 Finite difference solution to the flow between two rotating spheres. *Comp. Fluids* **12**, 77.

Fenstermacher, P. R., Swinney, H. L. & Gollub, J. P. 1979 Dynamical instabilities and the transition to chaotic Taylor vortex flow. *J. Fluid Mech.* **94**, 103.

Gorman, M. & Swinney, H. L. 1982 Spatial and temporal characteristics of modulated waves in the circular Couette system. *J. Fluid Mech.* **117**, 123.

King, G. P., Li, Y., Lee, W. & Swinney, H. L. 1984 Wave speeds in wavy Taylor-vortex flow. *J. Fluid Mech.* **141**, 365.

Krause, E. 1980 Taylor–Görtler vortices in spherical gaps. *Comp. Fluid Dyn.* **2**, 81.

Munson, B. R. & Menguturk, M. 1975 Viscous incompressible flow between concentric rotating spheres. Part 3. Linear stability and experiments. *J. Fluid Mech.* **69**, 705.

Nakabayashi, K. 1976 Study on the flow between rotating spheres, 1st report, Theoretical study. *Trans. Japan Soc. Mech. Engrs* (in Japanese) **42**, 1839.

Nakabayashi, K. 1978 Frictional moment of flow between two concentric spheres, one of which rotates. *Trans. ASME* I: *J. Fluids Engng* **100**, 281.

Nakabayashi, K. 1983 Transition of Taylor–Görtler vortex flow in spherical Couette flow. *J. Fluid Mech.* **132**, 209.

Nakabayashi, K., Nishida, H. & Onishi, S. 1981 Numerical studies of the flow between two concentric rotating spheres in the great range of Reynolds numbers. *Bull. Japan Soc. Mech. Engrs* **24**, 1787.

Newhouse, S., Ruelle, D. & Takens, F. 1978 Occurrence of strange Axion A attracters near quasi-periodic flows on T^m, $m > 3$. *Commun. Math. Phys.* **64**, 35.

Sato, H. & Saito, H. 1975 Fine-structure of energy spectra of velocity fluctuations in the transition region of a two dimensional wake. *J. Fluid Mech.* **67**, 539.

Sawatzki, O. & Zierep, J. 1970 Das Stromfeld im Spalt zwischen zwei konzentrischen Kugelflächen, von denen die innere rotiert. *Acta Mechanica* **9**, 13.

Schrauf G. 1986 The first instability in spherical Taylor–Couette flow. *J. Fluid Mech.* **166**, 287.

Schrauf, G. & Krause, E. 1984 Symmetric and asymmetric Taylor vortices in a spherical gap. In *Laminar–Turbulent Transition* (ed. V. V. Kozlov), p. 659. Springer.

Townsend, A. A. 1984 Axisymmetric Couette flow at large Taylor numbers. *J. Fluid Mech.* **144**, 329.

Tuckerman, L. S. 1983 Formation of Taylor vortices in spherical Couette flow. PhD thesis, Massachusetts Institute of Technology.

Waked, A. M. & Munson, B. R. 1978 Laminar–turbulent flow in spherical annulus. *Trans. ASME* I: *J. Fluids Engng* **100**, 281.

Walden, R. W. & Donnelly, R. J. 1979 Re-emergent order of chaotic circular Couette flow. *Phys. Rev. Lett.* **42**, 301.

WIMMER, M. 1976 Experiments on a viscous fluid flow between concentric rotating spheres. *J. Fluid Mech.* **78**, 317.

YAHATA, H. 1978 Temporal development of the Taylor vortices in a rotating fluid. *Prog. Theor. Phys. Suppl.* **64**, 165.

YAHATA, H. 1979 Temporal development of the Taylor vortices in a rotating fluid. II. *Prog. Theor. Phys.* **61**, 791.

YAHATA, H. 1980 Temporal development of the Taylor vortices in a rotating fluid. III. *Prog. Theor. Phys.* **64**, 782.

YAVORSKAYA, I. M., BELYAEV, YU. N., MONAKHOV, A. A., ASTAF'EVA, N. M., SCHERBAKOV, S. A. & VVEDENSKAYA, N. D. 1980 Stability, nonuniqueness and transition to turbulence in the flow between two rotating spheres. *Rep. no.* 595. Space Research Institute of the Academy of Science, USSR.